



Article

The state of platinum in pyrrhotite: X-ray absorption spectroscopy study and implications for the role of Fe sulfides as platinum carriers

Olga N. Filimonova¹, Alexander L. Trigub², Maximilian S. Nickolsky¹, Dmitriy A. Chareev³, Kristina O. Kvashnina^{4,5,6}, Elena V. Kovalchuk¹, Ilya V. Vikentyev¹, Vladimir L. Reukov¹ and Boris R. Tagirov^{1*} 

¹Institute of Geology of Ore Deposits, Petrography, Mineralogy and Geochemistry (IGEM RAS), 35, Staromonetnyi per., 119017 Moscow, Russia; ²National Research Centre “Kurchatov Institute”, 1, Akademika Kurchatova pl., 123182 Moscow, Russia; ³Institute of Experimental Mineralogy (IEM RAS), 142432 Chernogolovka, Moscow Region, Russia; ⁴ESRF - The European Synchrotron, CS40220, 38043 Grenoble Cedex 9, France; ⁵Helmholtz-Zentrum Dresden-Rossendorf (HZDR), Institute of Resource Ecology, P.O. Box 510119, 01314 Dresden, Germany; and ⁶Lomonosov Moscow State University, Department of Chemistry, GSP-1, Leninskie Gory, Moscow, 119991, Russia

Abstract

Pyrrhotite Fe_{1-x}S is the main sulfide component of platinum-group element (PGE) ores and commonly contains from a few tenths to a few dozen ppm of disseminated Pt. Here we report an X-ray absorption spectroscopy investigation into the state of Pt in synthetic pyrrhotite in combination with theoretical spectra modelling. The pyrrhotite crystals were obtained by means of the salt flux technique, using a eutectic mixture of alkali metal halides as the transport media. Analysis of the chemical composition of synthesised crystals showed that an increase of the temperature and sulfur fugacity yields higher concentrations of Pt in pyrrhotite. The Pt content reached 0.6 wt.% at the maximum temperature and sulfur fugacity ($t = 720^\circ\text{C}$, $\log f_{\text{S}_2} = -0.1$) achieved in a Pt-saturated system. X-ray absorption near-edge structure (XANES) analysis of Pt L_3 -edge spectra revealed that Pt is present in pyrrhotite in the 4+ and 2+ ‘formal’ oxidation states. Theoretical modelling of XANES and interpretation of extended X-ray absorption fine structure (EXAFS) spectra showed that Pt^{4+} substitutes for Fe in the crystal lattice of pyrrhotite, whereas Pt^{2+} forms PtS-like clusters disseminated in the pyrrhotite matrix. Atoms of isomorphous Pt^{4+} are surrounded by 6 S atoms at a distance of $2.39 \pm 0.02 \text{ \AA}$. According to theoretical simulations using the *FDMNES* program, the second coordination sphere of the solid-solution Pt contains one vacancy in the Fe sublattice within the Fe-layer. The Pt^{2+}S -like clusters can be considered as a quench product. High sulfur fugacity stabilises the solid-solution Pt and prevents the formation of the PtS-like clusters during cooling. The maximum content of the solid-solution Pt in pyrrhotite is ca. 50 times lower than in pyrite and can be approximated by a straight line in the $\log C(\text{Pt})$ vs. $1/T$ plot, it increases from 1 ppm at 350°C to 3 wt.% at 900°C .

Keywords: platinum, pyrrhotite, solid solution, solubility, cooperite, X-ray absorption spectroscopy

(Received 19 July 2021; accepted 5 October 2021; Accepted Manuscript published online: 26 October 2021; Associate Editor: František Laufek)

Introduction

In ores containing platinum-group elements (PGE), these metals can exist as: (1) discrete minerals – natural alloys and solid solutions; (2) intermetallic compounds of various compositions; (3) compounds with chalcogens (S, Se and Te) and metalloids (As, Sb and Bi); and (4) in the ‘invisible’ state (by analogy with ‘invisible’ Au) being disseminated in the matrix of the main ore-forming sulfide minerals (Distler *et al.*, 1977; Cabri, 1992; Barnes *et al.*, 2006). The latter form of occurrence is considered a solid solution of PGE and the base-metal sulfides and comprises an economically important (up to dominant) part of the total

PGE budget (e.g. Distler *et al.*, 1999; Cabri *et al.*, 2003). Pyrrhotite Fe_{1-x}S belongs to the main ore mineral assemblages in most magmatic sulfide PGE and nickel deposits, including the gigantic deposits of the Norilsk group, Russia; Bushveld Complex, South Africa; Great Dyke, Zimbabwe; Duluth, USA; Sudbury, Canada; Jinchuan, China; and Mt Keith, Australia, as well as a large Stillwater deposit, USA. In particular, the concentration of Pt in pyrrhotite in the ores of the Norilsk group deposits varies from ~0.1 to 40 ppm depending on the ore type and mineral assemblage (e.g. Sluzhenikin *et al.*, 1994; Distler *et al.*, 1999; Sluzhenikin *et al.*, 2015; Sluzhenikin *et al.*, 2020). These values of Pt concentration are consistent with Pt content in pyrrhotites from various other PGE deposits worldwide (Table 1), where the measured Pt content in pyrrhotite commonly ranges from a few tenths of ppm to several dozen ppm. Experimental studies of the solubility of Pt in pyrrhotite (Malevsky *et al.*, 1977; Majzlan *et al.*, 2002; Makovicky *et al.*, 1988, 1990, 1992; Ballhaus and Ulmer, 1995) showed that the

*Author for correspondence: Boris R. Tagirov, Email: boris1t@yandex.ru

Cite this article: Filimonova O.N., Trigub A.L., Nickolsky M.S., Chareev D.A., Kvashnina K.O., Kovalchuk E.V., Vikentyev I.V., Reukov V.L. and Tagirov B.R. (2021) The state of platinum in pyrrhotite: X-ray absorption spectroscopy study and implications for the role of Fe sulfides as platinum carriers. *Mineralogical Magazine* 85, 846–861. <https://doi.org/10.1180/mgm.2021.76>

Table 1. Content of Pt in pyrrhotites and their approximate formation/synthesis temperatures for ore deposits of various types and for model systems.

Pyrrhotite generation process		Temperature level	Deposit type	Max. C _{pt} (ppm)	Deposit	References							
Genetic type	Subtype												
Ortho-magmatic	Exsolution from S-rich monosulfide solid solution on cooling	Very high	(Cu-Ni)-Cr-PGE	11.9	Bushveld Complex, South Africa	Merensky Reef	Cabri <i>et al.</i> (2008) Godel <i>et al.</i> (2007) Osbaht <i>et al.</i> (2013) Mansur and Barnes (2020)						
				14.34									
				28.27									
				17.889									
				1.03				UG2 Reef Platreef	Osbaht <i>et al.</i> (2014) Holwell and McDonald (2007), Holwell <i>et al.</i> (2017)				
				3.34									
				0.01				Northern Bushveld	Smith <i>et al.</i> (2014)				
				10.5									
				2.185									
				0.21				Uitkomst Complex, South Africa	Trubač <i>et al.</i> (2018)				
				0.18				Beni Bousera, Northern Morocco	Piña <i>et al.</i> (2013)				
				High				Direct crystallisation from komatiitic magma	High	Cu-Ni (PGE)	340	Ivrea Verbano Zone, N. Italy Tolbachik volcano, Kamchatka, Russia Sudbury Complex, SE Canada Mirabela, Brazil Jinchuan, Central China Rosie Nickel, West Australia Voisey's Bay, SE Canada Duluth Complex, NE USA Alexo, SE Canada	Zaccarini <i>et al.</i> (2014) Zelenski <i>et al.</i> (2017) Dare <i>et al.</i> (2010, 2011, 2014) Knight <i>et al.</i> (2017) Chen <i>et al.</i> (2015) Godel <i>et al.</i> (2012) Amaral, (2017) Samalens <i>et al.</i> (2017) Mansur <i>et al.</i> (2021)
											15.5		
											0.5		
											1.58		
0.091													
1.544													
0.012													
0.57													
0.146													
14.75	J-M Reef, Stillwater Complex, Mid-West USA	Godel and Barnes (2008) Mansur and Barnes (2020)											
0.545													
5.41			Lac des Iles Complex, SE Canada		Djon and Barnes (2012) Duran <i>et al.</i> (2016)								
0.056													
20.79	Penikat, Finland	Barnes <i>et al.</i> (2008)											
3.606	Great Dyke, South Africa	Barnes <i>et al.</i> (2008) Piña <i>et al.</i> (2016) Oberthür <i>et al.</i> (1997)											
2.02													
64													
Late magmatic/ post magmatic	Crystallisation via replacement or sulfurisation	High to intermediate	Cu-Ni-PGE	44	Norilsk ore district, North Siberia, Russia	Norilsk-1	Distler <i>et al.</i> (1999) Barnes <i>et al.</i> (2006) Barnes and Ripley (2016) Mansur <i>et al.</i> (2020, 2021) Sluzhenikin <i>et al.</i> (2020)						
				27.2									
				10.24									
				2.743									
				8.13									
				2				Oktyabrsk	Cabri (1992) Mansur <i>et al.</i> (2020, 2021)				
				0.312									
				0.679				Talnakh	Mansur <i>et al.</i> (2020, 2021)				
				0.034				Aguablanca, Spain Fedorov, Kola, Russia	Piña <i>et al.</i> (2012) Cabri <i>et al.</i> (2010)				
				0.045									
Post magmatic	Fluid-related crystallisation	Intermediate	Cu-Co (+Au) vein	0.06	Pyshminsk-Klyuchevsk, Middle Urals, Russia Gumeshevsk, Middle Urals, Russia Sukhoi Log, South Siberia, Russia Rainbow, North Central Atlantic	Vikent'ev <i>et al.</i> (2010), Murzin <i>et al.</i> (2011) Vikentyev <i>et al.</i> (2005) Large <i>et al.</i> (2007) Bogdanov <i>et al.</i> (1999, 2002)							
			Skarn-copper-porphyry	0.064									
			Orogenic gold quartz-sulfide	0.05									
			Hydrothermal submarine massive sulfides	600									
Lab experiments	Stepped annealing of pure components	1100°C/ 1 bar	Model of magmatic system	49,900	Pt-Fe-S system Pt-Fe-S system Pt-Fe-As-S system	Majzlan <i>et al.</i> (2002) Makovicky <i>et al.</i> (1988) Makovicky <i>et al.</i> (1990, 1992)							
		900°C/ 1 bar											
		850°C/ 1 bar											
		470°C/ 1 bar		4400									
	Piston cylinder apparatus	810°C/ 10 kbar 800°C/ 10 kbar 720°C/ 10 kbar 680°C/ 10 kbar 600°C/ 10 kbar 560°C/ 10 kbar 450°C/ 10 kbar	Model of Cu-Ni-PGE magmatic system – experimental analogue of the Merensky Reef ores	11,000	Pt-Fe-S system	Ballhaus and Ulmer (1995)							
				6500									
				3400									
				2200									
				900									
				800									
450													

Pt content increases sharply with temperature and can reach ca. 0.5 wt.% at 1100°C (Table 1). The form of Pt occurrence in pyrrhotite, however, is still under debate.

The present study aims to determine the state (local atomic environment, position in the host mineral structure and valence state) of Pt in pyrrhotite using X-ray absorption spectroscopy (XAS) experiments combined with the theoretical spectra modelling. An X-ray absorption spectrum comprises an X-ray absorption near-edge structure part (XANES, to 50–80 eV from the absorption edge) that provides information about the electronic structure and coordination geometry (Mottana, 2004), and an extended X-ray absorption fine structure part (EXAFS, to 1000 eV from the absorption edge), that enables the determination of the type of neighbouring atoms, coordination numbers and the radii of coordination spheres around the absorbing atom (Galoisy, 2004). In order to determine the crystal-chemical properties of Pt in pyrrhotite, we synthesised pyrrhotite crystals doped with Pt at 650–720°C in systems of varying sulfur fugacity ($\log f_{S_2}$, from -7 to -0.8 at 650°C, and equal to -0.1 at 720°C). The use of synthetic crystals with elevated concentrations of Pt enabled us to acquire XANES spectra and obtain good quality EXAFS spectra and, as a result, properly characterise the local atomic environment of the dopant. The experimental X-ray absorption spectra were compared to simulated spectra to confirm the results of the spectra treatment and evaluate the number of vacant cationic positions near the Pt atom. Our experiments show that Pt in pyrrhotite can form an isomorphous solid solution that partly decomposes upon cooling. The factors which promote the formation of Pt-rich pyrrhotite solid solution are analysed and applied to the interpretation of the state of Pt in natural ores.

Materials and methods

Synthesis of minerals in the Pt–Fe–S system

Platinum-doped pyrrhotite and co-existing pyrite crystals were synthesised using a salt flux technique at a steady-state temperature gradient (Chareev *et al.*, 2016); the scheme of the experiment is given in Fig. 1. The synthesis parameters and the charge compositions are given in Table 2. The initial reagents were pre-synthesised $Fe_{0.9}S$ and FeS_2 powders, crystalline S, and Pt wire of 0.5 mm diameter. The starting materials were loaded into silica glass ampoules (8 mm ID, 11 mm OD and ~ 110 mm length). The length of Pt wire never exceeded half of the ampoule to prevent the growth of the crystals on the wire near the cold end. Then the eutectic salt mixtures listed in Table 2 were loaded to fill the maximum possible ampoule volume. The compositions of the salt mixtures were chosen according to the required synthesis temperature as described in Chareev (2016). The ampoules were evacuated, sealed with an oxygen torch gas burner, and placed into horizontal tube furnaces, which were then heated to the synthesis temperature. The experimental temperatures were 790°C hot end /720°C cold end (No. 5602), 710/650°C (Nos. 5590, 5592, 5599 and 5601).

Duration of the experiments varied from 2 to 8 weeks. During the experiment, the Pt-doped pyrrhotite and co-existing pyrite crystallised at the cold end of the ampoules. The ampoules were extracted from the furnaces and quenched in cold water at the end of the experiments. The cold ends of the ampoules were cut off, the synthesised crystals (~ 0.5 g) were washed in distilled water and then in acetone using an ultrasonic bath. To avoid

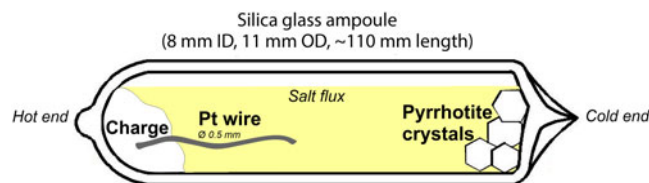


Fig. 1. Set-up of pyrrhotite synthesis: silica glass ampoule loaded with initial materials (charge) + salt flux. The Pt wire is at the hot side of the ampoule.

oxidising, the rinsed crystals were dried at 70°C in a muffle furnace for a few minutes.

Analytical methods

The phase composition of the synthesised crystals was determined by X-ray diffraction (XRD) using an EMPYREAN X-ray diffractometer ($CuK\alpha$, 45 kV, 40 mA and 0.033° step size) with subsequent comparison of the experimental diffraction patterns with database records. The measurements of pyrrhotite patterns were performed using a standard Bragg–Brentano (parafocusing) geometry, two wavelengths with a doublet intensity ratio of 2:1 were taken into account: $\lambda = 1.5406$ and $\lambda = 1.5444$ Å.

Several grains of pyrite and pyrrhotite from each sample were mounted in epoxy resin, polished and studied using reflected light optical microscopy (Olympus BX-51). Further analysis was undertaken using a JSM-5610LV scanning electron microscope (SEM) equipped with an X-Max 80 energy dispersive spectrometer (EDS). Crystals of pyrite and pyrrhotite were analysed for major elements (S and Fe) and minor element (Pt) using a JEOL JXA-8200 WD/ED combined electron probe microanalyser (EPMA) equipped with five wavelength dispersive X-ray spectrometers.

The Pt (^{195}Pt isotope) concentration was determined using laser ablation inductively coupled plasma mass spectrometry (LA-ICP-MS) on a Thermo X Series2 quadrupole ICP-MS coupled with a New Wave 213 laser. The in-house pyrrhotite $Fe_{0.9}S$ and sulfide reference material MASS-1 (Wilson *et al.*, 2002) were used as external standards. The in-house reference of $Fe_{0.9}S$ containing ~ 20 ppm Pt was obtained using the Wohlgemuth–Ueberwasser *et al.* (2007) experimental technique and calibrated with respect to the concentration of Pt against standards prepared by J.H.G. Laflamme and A. Peregoedova at the University of Québec at Chicoutimi. The ^{33}S and ^{57}Fe isotopes were used as internal standards. The EPMA and LA-ICP-MS operating conditions are given in Supplementary Table A.1 and Table A.2, respectively (see below for Supplementary material access).

X-ray absorption spectroscopy (XAS)

Several pyrrhotite crystals from each sample were selected for XAS experiments using a binocular microscope. The XRD patterns of these crystals correspond to pure pyrrhotite (PDF#24-0220, powder diffraction file from the International Centre for Diffraction Data, <https://www.icdd.com/>). The TFY-XAS (total fluorescence yield mode) experiments were performed at the Rossendorf Beamline BM20 at the European Synchrotron Radiation Facility (ESRF) in Grenoble, France. The storage-ring operating conditions were 6.0 GeV and 80–100 mA. The photon energy was scanned using the Si(111) monochromator. Rejection of higher harmonics was achieved by three Rh-coated mirrors working under total reflection. The 13-element high-throughput Ge-detector was used. All the

spectra were recorded at ambient temperature. The spectra of Pt_(cr), PtS_(cr), and PtS_{2(cr)} as reference substances were collected in transmission mode. The energy calibration was performed using a Pt foil (maximum of the first derivative, 11,564 eV). Energy scans from 11,250 to 12,600 eV were recorded and then averaged for each sample (the number of scans varied from 3 to 20). For the measurements, the pyrrhotite crystals and the reference materials (except Pt foil) were ground, and then powders were spread on an adhesive Kapton tape.

Analyses of X-ray absorption spectra

Data reduction and modelling of Pt L₃-edge absorption spectra were performed using the *Athena* (preliminary data processing, analysis of XANES spectra) and *Artemis* (EXAFS spectra fitting) programs of the *IFEFFIT* software package (Ravel and Newville, 2005).

XANES spectra analysis

Preliminary data processing included energy calibration, determination of the position of the absorption edge (e.g.) and the first intense feature (white line, WL), background subtraction and normalisation of the spectra. The position of the absorption edge is sensitive to the local atomic geometry and the oxidation state of the absorbing atom. Therefore, the experimental spectra of Pt-bearing pyrrhotites were compared to the spectra of reference materials with a known local atomic environment and 'formal' oxidation states of Pt: 0 (Pt), 2+ (PtS), 4+ (PtS₂). The 'formal' charge concept assumes that the chemical bonding in a compound is purely ionic. In the case of Pt-bearing phases with the substantial covalent component of the chemical bonding, the real atomic charge is different from the 'formal' one (Evstigneeva *et al.*, 2021). Even though purely ionic crystals do not exist, we use the 'formal' charges to discriminate between the Pt²⁺ in 4-fold coordination and Pt⁴⁺ in 6-fold coordination.

Linear Combination Fitting (LCF) analysis was carried out in the energy range between 11,550 and 11,625 eV using the *Athena* program.

EXAFS spectra analysis

The EXAFS spectra fitting provides information about the local atomic environment of the excited atom: the numbers of neighbouring atoms (N_{ij}), interatomic distances (R_{ij}), and Debye-Waller factors reflecting the static or thermal disorder (σ_{ij}^2). These parameters were determined via the non-linear least-squares fitting of experimental data with the theoretical spectra described by the EXAFS equation:

$$\chi_i(k) = S_{0i}^2 \sum_{j=1}^n \frac{N_{ij} F_{ij}(k)}{R_{ij}^2 k} e^{-\frac{2R_{ij}}{\lambda(k)}} e^{-2\sigma_{ij}^2 k^2} \sin(2kR_{ij} + \varphi_{ij}(k)). \quad (1)$$

The other parameters ($\lambda(k)$ – photoelectron mean free path length, $F_{ij}(k)$ – amplitude, $\varphi_{ij}(k)$ – phase shift) necessary to simulate theoretical spectra were calculated *ab initio* using the *FEFF6* program (Zabinsky *et al.*, 1995).

Theoretical modelling using the *ab initio* finite difference method for near-edge structure (FDMNES) code

The objective of the simulations was to study the state of Pt in the ideal NiAs-type pyrrhotite structure. Simulations of Pt L₃-edge XANES spectra were performed via theoretical modelling using the *ab initio* finite difference method for near-edge structure (FDMNES) code (Joly, 2001; Guda *et al.*, 2015). In

the FDMNES program, the molecular field is considered as a superposition of three fields: (1) atoms for which potentials are approximated as spherically symmetric, (2) an intersphere (muffin-tin) region, and (3) space with effective potential following Hedin and Lundqvist (1971) using the local density approximation (LDA). The cubic FeS₂ crystal structure (space group Pa $\bar{3}$ and lattice parameter $a = 5.4179$ Å; Brostigen and Kjekshus, 1969) and the hexagonal Fe_{1-x}S crystal structure (space group P6₃mc, lattice parameters $a = 3.4300$ Å, $c = 5.6800$ Å and $a/c = 1.6560$; Wyckoff, 1963) were used as initial structures in all calculations. Simulations were performed with a 6 Å cluster radius and a 3 × 3 × 3 supercell structure of pyrite (reference material), and a 6 Å cluster radius and a 3 × 3 × 2 supercell structure of pyrrhotite (samples). Convolution parameters obtained for simulated XANES spectrum of isomorphous Pt in pyrite were used for the convolution of simulated Pt-bearing pyrrhotite spectra (the spectrum and parameters for the local atomic environment of isomorphous Pt in pyrite were adopted from Filimonova *et al.*, 2019). The interpretation was carried out via the comparison of XANES simulated spectra with those obtained in the experiment.

Results and discussion

The concentration and distribution of Pt in pyrite and pyrrhotite

The products of synthesis experiments consisted of crystals with a grain size of 0.5–5 mm. A few crystals of each sample were examined using SEM/EDS, EPMA and LA-ICP-MS methods. Phase and chemical compositions of synthesis products are given in Table 2 and Supplementary Table A.3. The content of Pt in pyrite co-existing with pyrrhotite varies between 0.13 and 0.26 at.% in samples synthesised at the temperature of 650°C, and in pyrrhotite from 0.004 to 0.12 at.% (temperature interval 650–720°C). The concentration of Pt in pyrrhotite drops with decreasing temperature.

Back-scattered electron (BSE) photomicrographs in Fig. 2 display selected synthesised crystals. Analysis of SEM images revealed the presence of microcrystals of Pt-bearing pyrrhotites in the pyrite crystals. At the same time, pyrrhotite crystals are free of inclusions of pyrite and Pt-bearing phases. The BSE images demonstrate the uniform Z contrast within the distinct zones of the pyrite crystals and within the single crystals of pyrrhotites. Time-resolved LA-ICP-MS spectra exhibit the smooth shape of the signal ablated within distinct crystal zones, which confirms the homogeneous character of synthesised Pt-doped pyrrhotite and co-existing pyrite crystals (Fig. 3 and Supplementary Fig. A.1).

The compositions of the synthesised pyrrhotite samples are shown in the log f_{S_2} vs. 1000/T plot in Fig. 4. The binary plot shown in Fig. 5 demonstrates a negative dependence between the concentration of major (Fe) and trace (Pt) elements determined by EPMA of selected pyrrhotite samples. As follows from Fig. 4 and Fig. 5, the increase of sulfur fugacity and synthesis temperature increases Pt content in pyrrhotite. This behaviour of Pt – increase in solubility with increase of the S₂ fugacity and temperature – is consistent with the solid-solution formation in the Pt–Fe–S system.

The 'formal' oxidation state of Pt in pyrrhotite from qualitative analysis of XANES

The Pt L₃-edge XANES spectra of Pt-bearing pyrrhotites are shown in Fig. 6a together with spectra of references: Pt_(cr), PtS_(cr), PtS_{2(cr)}.

Table 2. Parameters of synthesis, starting materials, compositions and empirical formulae of synthetic pyrrhotite and co-existing pyrite crystals.

Sample No. (synthesis temperature, °C at the hot/cold end of the ampoule)	Starting materials	Eutectic salt mixture composition (duration of synthesis, weeks)	Synthesis products ^a	Average Pt concentration in pyrrhotite ^b	Average Pt concentration in pyrite ^b	Empirical formula of Po and Py ^a
5601 (710/650)	FeS ₂ + Fe _{0.9} S + Pt _(cr)	RbCl/NaCl/KI/KBr (2)	Po + Py	wt.%: 0.28±0.19 at.%: 0.06±0.04	wt.%: 0.62±0.89 at.%: 0.13±0.19	(Fe,Pt) _{0.89} S + (Fe,Pt)S ₂
5602 (790/720)	FeS ₂ + Fe _{0.9} S + Pt _(cr)	KCl/NaCl (2)	Po + PtS ₂	wt.%: 0.54±0.16 at.%: 0.12±0.04	-	(Fe,Pt) _{0.88} S
5592 (710/650)	FeS ₂ + S + Pt _(cr)	CsCl/NaCl/KCl (2)	Po + Py	wt.%: 0.28±0.07 at.%: 0.06±0.04	wt.%: 0.95±1.79 at.%: 0.20±0.38	(Fe,Pt) _{0.89} S + (Fe,Pt)S ₂
5590 (710/650)	FeS ₂ + S + Pt _(cr)	CsCl/NaCl/KCl (2)	Po + Py	wt.%: 0.36±0.07 at.%: 0.08±0.02	wt.%: 1.24±1.54 at.%: 0.26±0.32	(Fe,Pt) _{0.89} S + (Fe,Pt)S ₂
5599 (710/650)	Fe _{0.9} S + Pt _(cr)	RbCl/NaCl/KI/KBr (2)	Po	wt.%: 0.02±0.01 at.%: 0.004±0.001 ^c	-	(Fe,Pt) _{0.975} S

^aPo – pyrrhotite, Py – pyrite; ^baverage concentration is determined using EPMA, standard deviation corresponds to ±2σ; ^cconcentration is determined via LA-ICP-MS analyses, standard error corresponds to ±2σ.

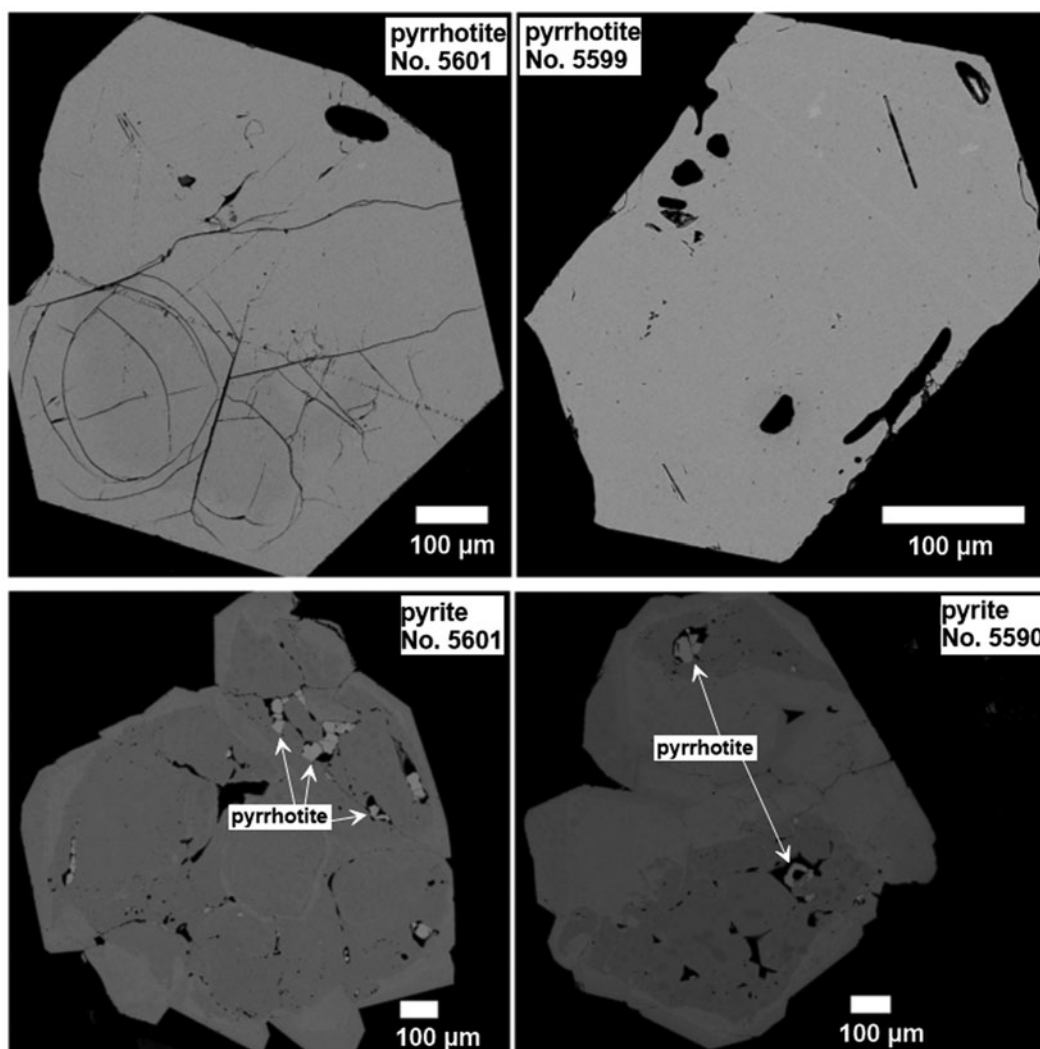


Fig. 2. Selected synthetic Pt-bearing pyrite and pyrrhotite crystals (Nos. 5590, 5601 and 5599). Back-scattered electron (BSE) images show (top) Pt-doped pyrites containing pyrrhotite inclusions (the distribution of Pt is uniform within growing zones of the crystals, the growing zones differ in the concentration of Pt), and (lower) a uniform Z-contrast distribution of Pt in pyrrhotites of low Pt content.

Positions of the absorption edge (e.j.), white line (WL), and the WL intensities are given in Table 3. The Pt L_3 -edge absorption is related to $2p \rightarrow 5d$ transitions. Therefore, the WL intensity is sensitive to the

number of empty states (holes) in the $5d$ valence orbitals. The increase of the WL intensity reflects the increase of the vacancies amount and can be attributed to the loss of electrons localised on

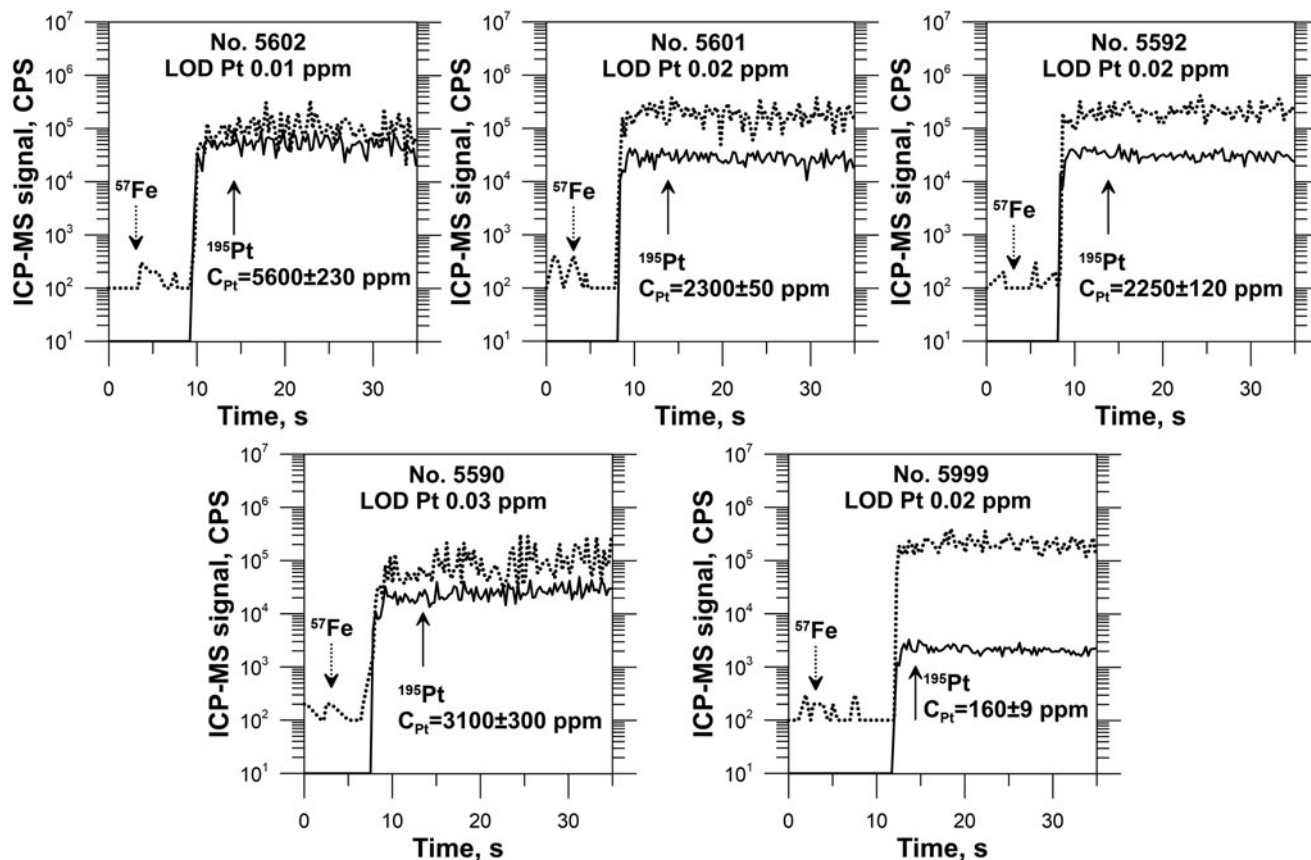


Fig. 3. Selected time-resolved laser ablation ICP-MS spectra of Pt-bearing pyrrhotites. Analyses were performed using a spot size of 60 μm . The Pt disseminated in the pyrrhotite matrix behaves similarly to the internal standard element, Fe. Uncertainty corresponds to $\pm 2\sigma$, limit of detection (LOD) is calculated using *lolite* (Paton *et al.*, 2011) and corresponds to 2σ confidence interval.

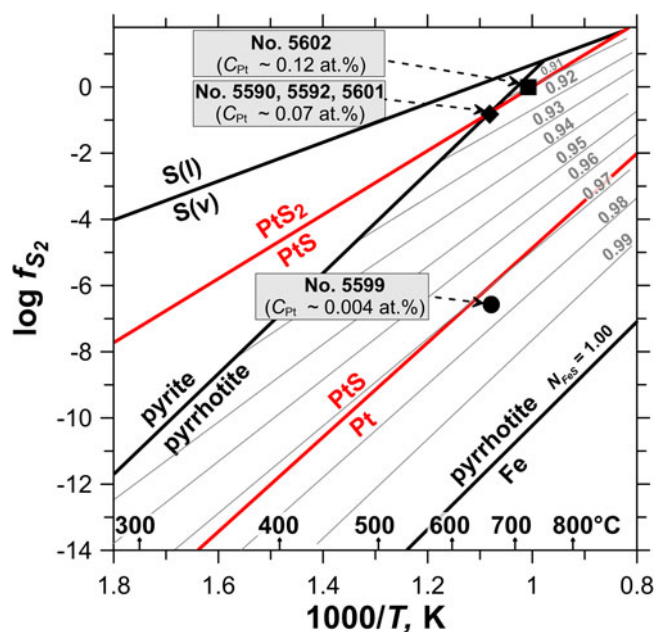


Fig. 4. The synthesis experiments parameters. Data are adopted from Toulmin and Barton (1964), Naumov *et al.* (1974) and Mills (1974) for FeS-S₂, Pt and PtS, PtS₂, respectively. The N_{FeS} indicates composition isopleths of pyrrhotite. The black symbols indicate the calculated values of sulfur fugacity in the experimental systems determined from the pyrrhotite composition.

the $5d$ orbitals. In general, the increase of the WL intensity for the related compounds means the increase of the positive charge of the absorbing atom (see Evstigneeva *et al.*, 2021 for discussion of the effect of the Pt charge on the parameters of spectral features). In addition, for more oxidised species, the absorption edge shifts to higher energy.

Before interpretation of XANES spectra, it is necessary to prove the absence of the signal from pyrite, which can contain important (up to a few wt.%) concentrations of Pt in solid solution form (Filimonova *et al.*, 2019). Optical microscopy, SEM and XRD analyses showed no contamination of the pyrrhotite samples studied with pyrite. However, the XRD method is not sensitive to the presence of low (<5% wt.%) concentrations of Pt-bearing pyrite. Comparison of the spectra of samples synthesised at different T - f_{S_2} conditions shows that the contribution of the signal from Pt-bearing pyrite is negligible. Indeed, XANES spectra of sample Nos. 5602 and 5601 are almost identical regardless of the fact that sample No. 5602 was synthesised in the pyrrhotite stability field (no pyrite present according to the $\log f_{\text{S}_2} - 1000/T$ diagram in Fig. 4), whereas sample No. 5601 was synthesised at pyrite + pyrrhotite equilibrium. Accordingly, the spectra of the synthesised crystals correspond to the Pt-bearing pyrrhotite. Further evidence of the absence of pyrite contamination is provided by the analysis of EXAFS spectra in the following section.

Compared with the spectra of model substances – $\text{Pt}^0_{(\text{cr})}$ and $\text{Pt}^{2+}\text{S}_{(\text{cr})}$, the main features of the spectra of pyrrhotite samples Nos. 5590, 5592, 5601 and 5602 are significantly more intense,

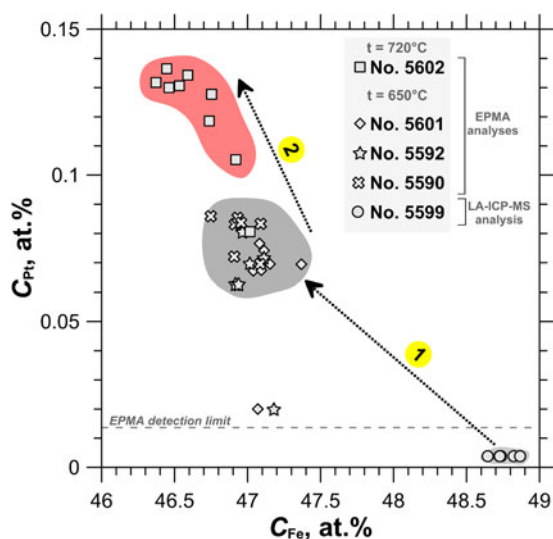


Fig. 5. The concentration of Pt as a function of Fe concentration determined by EPMA and LA-ICP-MS in the pyrrhotite samples used for the XAS experiments. Uncertainty of $\pm 2\sigma$ for each point never exceeds the filled fields, which show the variation of pyrrhotite compositions. Arrow 1: C_{Pt} increases up to 0.3 wt.% with increasing sulfur fugacity at constant temperature of 650°C. Arrow 2: C_{Pt} increases up to 0.5 wt.% with increasing temperature from 650°C to 720°C.

while their positions are shifted to higher energies. This means that the admixtures of $Pt^{0}_{(cr)}$ and $Pt^{2+}S_{(cr)}$ are absent in the samples. The charge of Pt exceeds the charge of the metal in the references. At the same time, the position of the e.j. and WL of Pt-bearing pyrrhotites and $Pt^{4+}S_{2(cr)}$ are similar within the measurement error of ± 0.5 eV. Moreover, the similarity of the spectra of Pt-bearing pyrrhotites and $PtS_{2(cr)}$ implies the local atomic geometry of Pt in the pyrrhotite samples to be close to $Pt^{4+}S_2$ where 6 S atoms surround the Pt atom. The intensities of WL (I_{WL}) of pyrrhotite spectra are somewhat below that of PtS_2 , which contains Pt in the 'formal' oxidation state of 4+ ($I_{WL}(PtS_2) = 1.67$ arbitrary units (a.u.), Table 3). Throughout the series of pyrrhotites studied, the WL intensity drops from 1.63 a.u. (sample Nos. 5601 and 5602) to 1.57–1.53 a.u. (sample Nos. 5590 and 5592). Hence, the positive charge of Pt decreases in the following sequence: $PtS_2 > Nos. 5601 \text{ and } 5602 > Nos. 5590 \text{ and } 5592$. We suggest that the observed decrease of the WL intensity in the series of samples can result from an admixture of Pt^{2+} .

Regardless of the fact that positions of the main spectral features of sample No. 5599 are similar to the other pyrrhotite spectra, the WL intensity of this spectrum decreases markedly in comparison with $PtS_{2(cr)}$ and other samples and increases significantly in comparison with $PtS_{(cr)}$ ($I_{WL} = 1.38$ a.u. for the sample vs. $I_{WL} = 1.25$ a.u. for $PtS_{(cr)}$). This observation may be accounted for by the presence of Pt in 4+ and 2+ 'formal' oxidation states of commensurable quantities.

Given the above analysis, we suggest that the XANES spectra of Pt in pyrrhotite samples result from the superposition of signals from two forms of Pt: Pt^{4+} in the form of a solid solution or $Pt^{4+}S_2$, and Pt^{2+} in the form of $Pt^{2+}S$ -like clusters or inclusions, of which size prevents detection by SEM/EDS and LA-ICP-MS methods.

Local atomic environment of Pt in pyrrhotite from EXAFS

The experimental Pt L_3 -edge EXAFS spectra and their Fourier transforms together with the fitting results are shown in Fig. 6b,c

(Pt-bearing pyrrhotites), and Supplementary Fig. A.2 (PtS_2 reference). The results of the spectra fitting are given in Table 4.

Comparison of the Fourier transforms of the EXAFS signal from Pt-bearing pyrites and pyrrhotites provides further evidence of the absence of the pyrite contamination. The Fourier transforms of the spectra of Pt-bearing pyrites clearly have a second coordination shell consisting of S + Fe + Pt atoms (Fig. 6c). In contrast, the Fourier transforms of Pt-bearing pyrrhotites are different: no distinctive peaks typical for Pt in pyrite are present between 2.3–4.3 Å. This means that the contribution from Pt-bearing pyrite is certainly negligible.

Regardless of the Pt concentration, the best fit of the experimental pyrrhotite spectra is achieved when Pt atoms are octahedrally coordinated by S atoms in the first coordination sphere. Our attempts to fit the weak contribution from the distant coordination sphere atoms failed to produce a set of consistent data. The reasons for the failure can stem from the presence of several forms of Pt or the nonstoichiometric composition of pyrrhotite. The absence of a contribution of heavy Pt atom in the second coordination sphere means the absence of the admixtures of submicrometre or nano-sized Pt, PtS and PtS_2 inclusions.

In the samples of Pt-bearing pyrrhotites, the Pt–S distance varies from 2.36 to 2.39 Å, and the number of atoms of S nearest to Pt from 4.7 to 6.2. The observed variations of interatomic distances and coordination numbers, as well as high fitting uncertainty of the values (see Table 4), can be explained by the presence of varying amounts of two forms of Pt: the Pt-bearing solid solution with coordination number $N_S = 6$, and PtS -like clusters with $N_S = 4$ and a smaller interatomic distance $R_{Pt-S} = 2.31$ Å. This assumption will be verified by LCF analysis of XANES spectra. To make results of EXAFS spectroscopy consistent with the XANES spectra analysis, the results of the EXAFS spectra fittings are discussed below in the order of the decrease of Pt oxidation state (from 4+ to 2+), which is traced by the decrease of the WL intensity given in the last column of Table 3.

In sample No. 5601 the absorbing atom is 6-fold coordinated with S atoms (PtS_6 octahedra), and the value of $R_{Pt-S} \approx 2.39$ Å is the maximum Pt–S distance among the pyrrhotite samples studied. Considering this, we suppose that Pt in this sample presents dominantly in the lattice-bound state as the isomorphous solid solution while the contribution of PtS -like clusters is negligible. In sample No. 5602 we observed a slight decrease of Pt–S interatomic distance and the first sphere coordination number relative to sample No. 5601. However, the similarity of XANES spectra of these two samples implies that in sample No. 5602 Pt also exists mainly in the solid-solution form.

Analysis of the EXAFS spectra of samples No. 5592 and 5590 reveals a slight decrease of coordination number and interatomic distances down to $N_S \approx 5.5$ and $R_{Pt-S} = 2.37$ – 2.36 Å, respectively, relative to sample No. 5601 where the Pt-bearing solid solution predominates. The decrease can stem from the formation of the second form of Pt – the PtS -like clusters. The formation of the clusters where Pt occurs in 2+ 'formal' oxidation state is consistent with the XANES spectra analysis.

For sample No. 5599 the considerable increase of the Debye–Waller parameter ($\sigma^2 = 0.007 \pm 0.007$ Å²), together with large uncertainties of the calculated values of N_S and R_{Pt-S} , can be explained by the presence of two forms of Pt – isomorphous solid solution (Pt^{4+}) and $Pt^{2+}S$ -like clusters – with concentrations are close to each other.

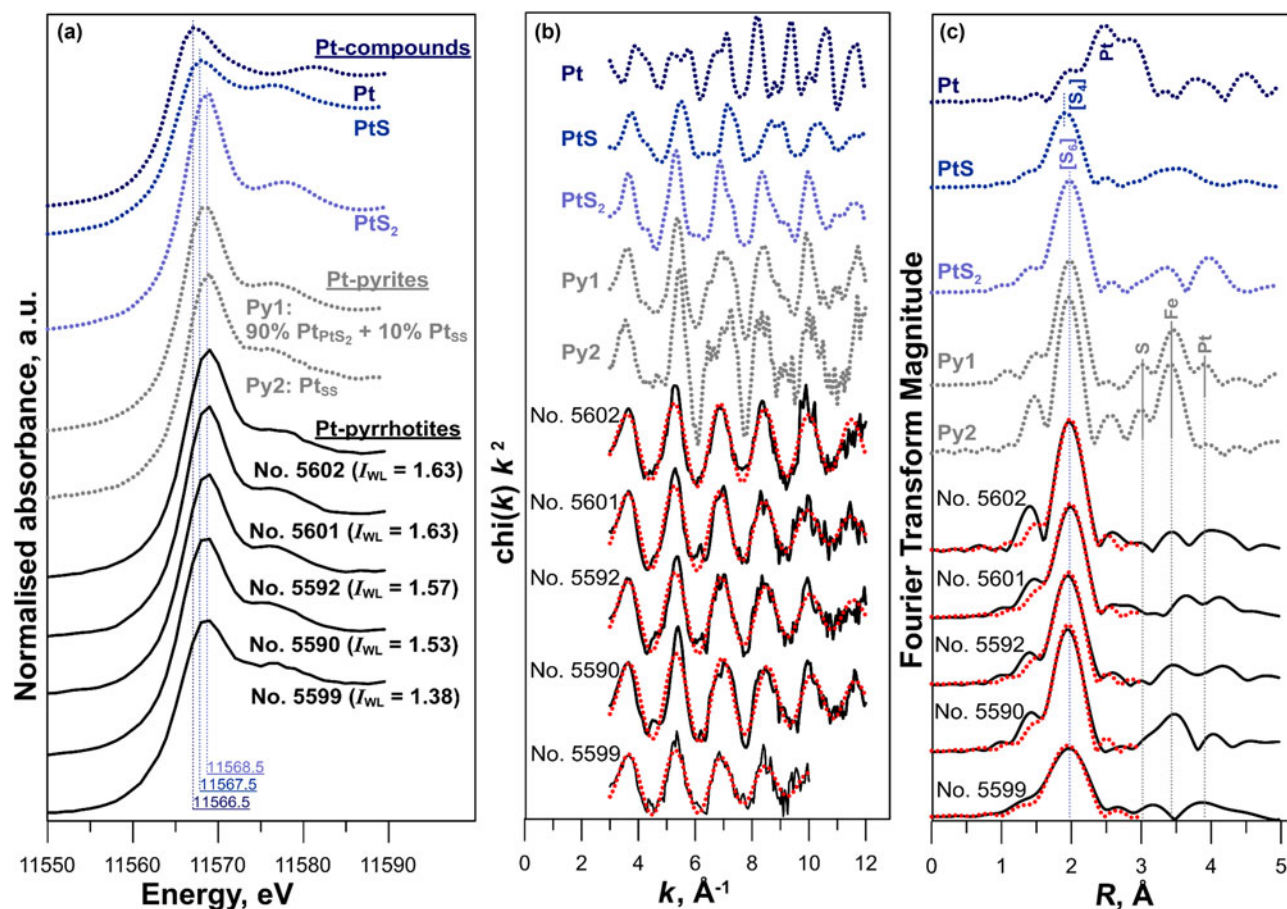


Fig. 6. (a) Normalised XANES spectra of Pt-bearing pyrite, pyrrhotite and reference materials. For Pt-bearing pyrites: Pt_{PtS₂} corresponds to nano-sized PtS₂ inclusions, Pt_{SS} – the solid solution Pt in pyrite (the spectra are adopted from Filimonova *et al.*, 2019). Vertical solid lines denote positions of the first intense feature (white line, WL) of pyrrhotites and references spectra. (b,c) the k^2 -weighted background-subtracted EXAFS spectra together with their Fourier transforms (not corrected for phase shift, black lines – experiment, dotted red lines – fitted results). Vertical lines indicate the approximate position of atoms and atomic groups surrounding Pt.

Theoretical FDMNES modelling of XANES spectra

To facilitate discussion of FDMNES calculation results, the Fe_{1–3}S structure and the cation local atomic environment are shown in Fig. 7. The pyrrhotite structure is represented by layers of hexagonal close-packed S atoms normal to the *c* axis. Full layers in which octahedra are occupied by Fe atoms alternate with the vacancy (or defective) layers. In the second coordination shell, metal atoms are surrounded by six Fe atoms at 3.43 Å (within each Fe layer) and two Fe atoms at 2.84 Å (within neighbouring Fe layers).

The spectrum of Pt-bearing pyrite (Pt in the isomorphous solid-solution state, Filimonova *et al.*, 2019) with EXAFS-determined parameters of a Pt local atomic environment up to ~4 Å was chosen as a reference. The calculated spectrum of the Pt-bearing pyrite is shown in Fig. 8a together with the experimental spectrum adopted from Filimonova *et al.* (2019). The parameters of convolution, optimised for Pt-bearing pyrite, were then used to model the XANES spectra of Pt-bearing pyrrhotite.

The calculations aimed to study the effect of coordination number N_s in the first coordination sphere, and the number of vacancies in cationic sublattice in the second coordination sphere on the shape of XANES spectra and positions of the spectral features. For these purposes, two series of calculations were

Table 3. Positions of absorption edge (e.j.), white line (WL), and WL intensity of Pt L_{3} -edge normalised spectra of standards and synthetic Pt-bearing pyrrhotites as determined by the *Athena* program. The uncertainty of the energy values is ± 0.5 eV.

Sample or standard	Feature	Position (eV)	WL intensity (a.u.)
Pt _(cr)	e.j.	11,564.0	1.27
	WL	11,566.5	
PtS _(cr)	e.j.	11,564.5	1.25
	WL	11,567.5	
PtS _{2(cr)}	e.j.	11,565.5	1.67
	WL	11,568.5	
No. 5601	e.j.	11,566.0	1.63
	WL	11,568.5	
No. 5602	e.j.	11,566.0	1.63
	WL	11,568.8	
No. 5592	e.j.	11,565.5	1.57
	WL	11,568.4	
No. 5590	e.j.	11,565.5	1.53
	WL	11,568.5	
No. 5599	e.j.	11,565.5	1.38
	WL	11,568.5	

performed. In the first, preliminary series, the interatomic distances varied from 2.33 to 2.39 Å, and the ‘best’ distance, which demonstrated the closest agreement between the calculated and

Table 4. The local atomic structure of Pt in PtS and Pt-bearing pyrrhotites determined by EXAFS k^2 -weighting spectra fitting using IFEFFIT package (fit in R -space). Numbers without uncertainties were fixed during the fit. Uncertainties were determined by the *Artemis* program.

Atom	N	R (Å)	σ^2 (Å ²)	E^0 (eV)	Fit quality:		Theoretical data ^b	
					Reduced χ^2	R -factor	R (Å)	N
PtS _(cr) (R -range: 1.3–4, k -range: 3–12)								
S	4	2.31±0.01	0.005±0.001	10.3±1.5	417.8	0.035	PtS	
Pt	4	3.49±0.05	0.011±0.005 ^c				2.31	4
Pt	8	3.87±0.07	0.011 ^c				3.47	4
S	8	4.09±0.03	0.007±0.005				3.92	8
No. 5601 (R -range: 1.3–2.3, k -range: 3–12)								
S	6.2±1.2	2.39±0.02	0.004±0.002	7.8±2.3	16.1	0.012	Fe _{1-x} S	
No. 5602 (R -range: 1.3–2.3, k -range: 3–12)								
S	4.7±1.7	2.38±0.02	0.001±0.003	6.7±4.3	71.0	0.033	Fe _{1-x} S	
No. 5592 (R -range: 1.3–2.3, k -range: 3–12)								
S	5.5 ±1.0	2.37±0.01	0.004±0.002	6.7±2.0	10.9	0.008	Fe _{1-x} S	
No. 5590 (R -range: 1.3–2.3, k -range: 3–12)								
S	5.6±1.0	2.36±0.01	0.003±0.002	6.8±2.0	31.1	0.008	Fe _{1-x} S	
No. 5599 (R -range: 1.3–2.3, k -range: 3–10)								
S	5.2±3.1	2.38±0.06	0.007±0.007	6.7±4.3	37.8	0.011	Fe _{1-x} S	

^aAmplitude reduction factor $S_0^2 = 0.90$ adopted from Filimonova *et al.* (2019); ^bPtS – Rozhdestvina *et al.* (2008); pyrrhotite Fe_{1-x}S – Wyckoff (1963); ^cDebye–Waller factors are fixed to be equal.

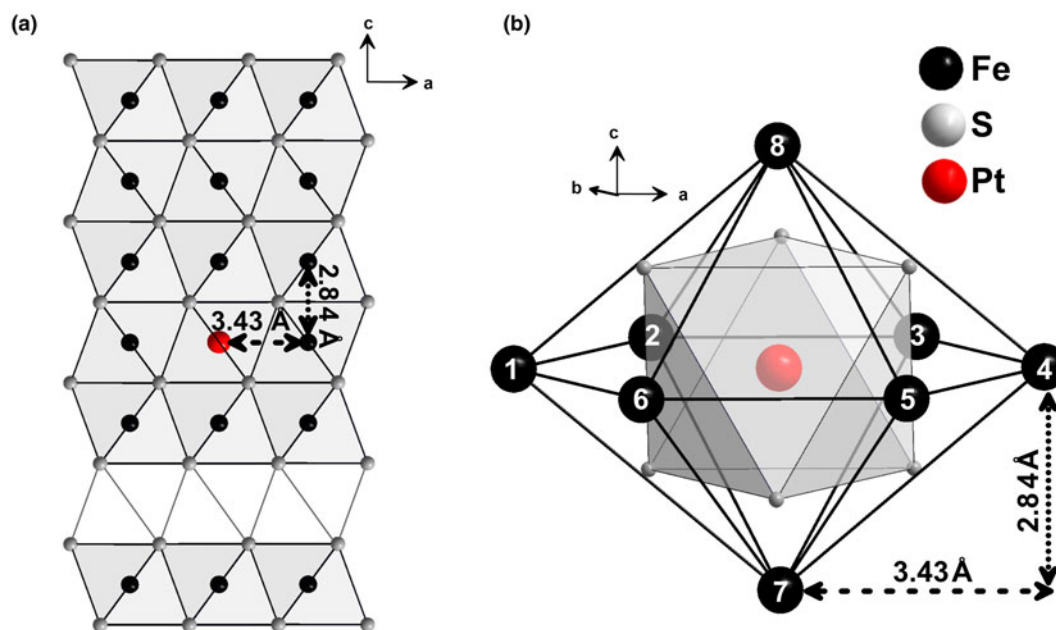


Fig. 7. (a) Crystal structure of Fe_{1-x}S. (b) Cation local atomic environment. The vacancies in the Fe sites are ordered: the vacancy layer alternates with full layers normal to c . Metal atoms are surrounded by six Fe atoms at 3.43 Å (within each Fe layer) and two Fe atoms at 2.84 Å (within the neighbouring Fe layer). Crystallographic data are adopted from Wyckoff (1963) and visualised using the program *DIAMOND* (Putz and Brandenburg, 2012).

experimental spectra of the solid solution Pt (sample No. 5601), was selected for further calculations. We fixed the ‘best’ Pt–S distance in the second series, but varied the number of S atoms in the first coordination sphere (from 6 to 4), and the number of vacancies in the second coordination sphere. The calculation results are shown in Supplementary Fig. A.3. The ‘best’ values are discussed below.

The effect of Pt–S distance on the calculated XANES

In this series, the coordination number was fixed as $N_s = 6$: Pt substitutes for Fe in the structure of pyrrhotite. Three calculations were performed for various interatomic distances with R_{Pt-S} values in the first coordination sphere of 2.33, 2.36 and 2.39 Å.

The simulated spectra are compared to the spectrum of sample No. 5601 containing only isomorphous Pt in Fig. 8b. The increase of the R_{Pt-S} distance resulted in a significant increase in the white line intensity (Fig. 8c). Additionally, due to a leftward shift (towards the lower energies) of the position of the second intense feature B (Fig. 8d) the energy difference ΔE between positions of the WL and peak B decreases with an increase of the Pt–S distance: $\Delta E(2.33 \text{ Å}) > \Delta E(2.36 \text{ Å}) > \Delta E(2.39 \text{ Å})$. Although none of the models describes all the features of sample No. 5601 spectrum precisely, we chose the interatomic distance, $R_{Pt-S} = 2.36 \text{ Å}$ for further calculations because the energy interval between the main (WL) and the second (B) features in the calculated and experimental spectra are identical (Fig. 8e). The difference

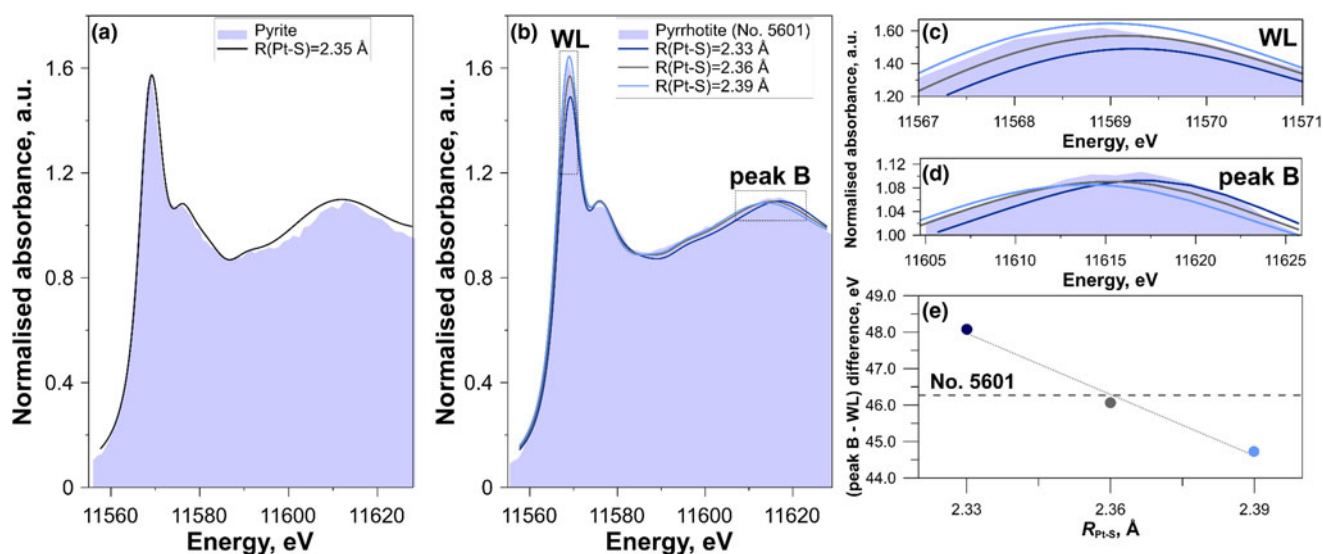


Fig. 8. (a) Experimental Pt L_{3} -edge XANES spectrum of the solid solution Pt in pyrite ($(\text{Fe,Pt})\text{S}_2$) (blue field, adopted from Filimonova *et al.*, 2019) shown together with the spectrum calculated by FDMNES code (solid line). The energy origin is defined relative to the theoretical Fermi level. (b) Experimental Pt L_{3} -edge XANES spectrum of sample No. 5601 – the solid solution Pt in pyrrhotite ($(\text{Fe,Pt})_{1-x}\text{S}$) (blue field, this study) shown together with the spectra of models with different Pt-S interatomic distances ($R_{\text{Pt-S}} = 2.33, 2.36$ and 2.39 Å) calculated by FDMNES code (solid lines). (c, d) Enlarged portions of spectra (b): WL and peak B region of Pt L_{3} -edge XANES, calculated and experimental spectra. **E:** The difference between peak B and WL (eV) as a function of the interatomic distance $R_{\text{Pt-S}}$ (Å), the dotted line corresponds to the regression through the experimental points. Circles - values obtained from calculated spectra, horizontal dashed line - value derived from the experimental spectrum No. 5601. The best fit of the experimental spectrum is obtained for Pt in the cation site surrounded by 6 S atoms at 2.36 Å.

between the values of $R_{\text{Pt-S}}$, determined by means of the XANES spectra simulations and EXAFS spectra fittings (2.36 Å vs. 2.39 Å), can be explained by the relatively high uncertainty of the theoretical XANES calculations method, which exceeds the uncertainty of the EXAFS spectra fitting procedure (± 0.02 Å for the first coordination sphere, Table 4). However, the accuracy of the FDMNES simulations is sufficient to study the composition of the first and second coordination spheres.

The effect of N_S (the first coordination sphere) and N_{Fe} (the second coordination sphere) on the calculated XANES

The ‘best’ simulated spectra are compared to the experimental ones in Fig. 9, and the ‘best’ models are presented in Table 5. Considering that Pt in pyrrhotite can exist in two forms: the isomorphous solid solution ($N_S = 6$) and PtS-like clusters ($N_S = 4$), we simulated XANES spectra for the first sphere coordination numbers $N_S = 6, 5$ and 4 . The decrease of the number of S atoms leads to the significant decrease of WL and peak B intensities of the simulated spectra (Supplementary Fig. A.3, calculations indicated by Nos. 1, 2 and 3). The spectra for Nos. 5601 and 5602 are best described by a model with Pt surrounded by 6 S atoms in the first coordination shell; Nos. 5590 and 5592 by 5 S atoms in the first coordination shell; and No. 5599 by 4 S atoms in the first coordination shell.

To test for the presence of Fe vacancies in the second shell around the excited Pt atom, the next series of simulations were performed for a model with one vacancy in the Fe site at $R_{\text{Pt-Fe}} = 3.43$ Å (within each Fe layer, atom Nos. 1–6 in Fig. 7), and for another model – one vacancy at $R_{\text{Pt-Fe}} = 2.84$ Å (within the neighbouring Fe layer, atom Nos. 7 and 8 in Fig. 7). The model with a vacancy in neighbouring Fe layer at a Pt–Fe distance of 2.84 Å (Supplementary Fig. A.3, calculations 7, 8 and 9) fails to reproduce the experimental spectra. The best agreement between the experimental and calculated spectra is achieved for the

models with a vacancy within the Fe layer at $R_{\text{Pt-Fe}} = 3.43$ Å (Supplementary Figure A.3, calculations 4, 5 and 6), or without vacancies. An attempt to use the models with two and three vacancies at $R_{\text{Pt-Fe}} = 3.43$ Å failed to describe the experimental spectra: the intensity and positions of the peaks of calculated spectra differ significantly from the experimental ones (Supplementary Fig. A.3, calculation Nos. 7, 8 and 9). Accordingly, the spectra of pyrrhotite samples Nos. 5601 and 5602 (Pt is in the solid-solution state) are best described by a model with $N_S = 6$ (first sphere) and $N_{\text{Fe}} = 7$ (second sphere, one vacancy at $R_{\text{Pt-Fe}} = 3.43$ Å). Formation of vacancies at $R_{\text{Pt-Fe}} = 2.84$ Å (within the neighbouring Fe layer) and more than one vacancy at $R_{\text{Pt-Fe}} = 3.43$ Å are ruled out.

The spectra of sample Nos. 5590 and 5592 are best described by a model with $N_S = 5$ and $N_{\text{Fe}} = 8$, and sample No. 5599 – by a model with $N_S = 4$ and $N_{\text{Fe}} = 8$. We note that the formation of the vacancy in the Fe site is not required to describe the experimental spectra of sample Nos. 5590, 5592 and 5599.

We tried to use the approach developed by Ballhaus and Ulmer (1995) to quantify the substitution of Pt in pyrrhotite using their empirical equation. The substitution mechanism suggested by Ballhaus and Ulmer (1995) requires 4 to 6 vacancies in the Fe sublattice around the Pt site in our samples. This mechanism can be ruled out for two reasons: (1) it seems unrealistic in terms of the charge balance requirements, and (2) it contradicts results of the FDMNES modelling, which showed that experimental spectra can be described by the model with no more than one vacancy in the Fe sublattice.

Linear Combination Fit (LCF) analysis of XANES

The LCF analysis of XANES spectra was performed to quantify the ratio of Pt in the solid-solution state (Pt_{ss}) to PtS-like clusters (Pt_{PtS}) in the samples of Pt-bearing pyrrhotite. We used the spectra of the pyrrhotite sample containing ~ 0.3 wt.% Pt (No. 5601,

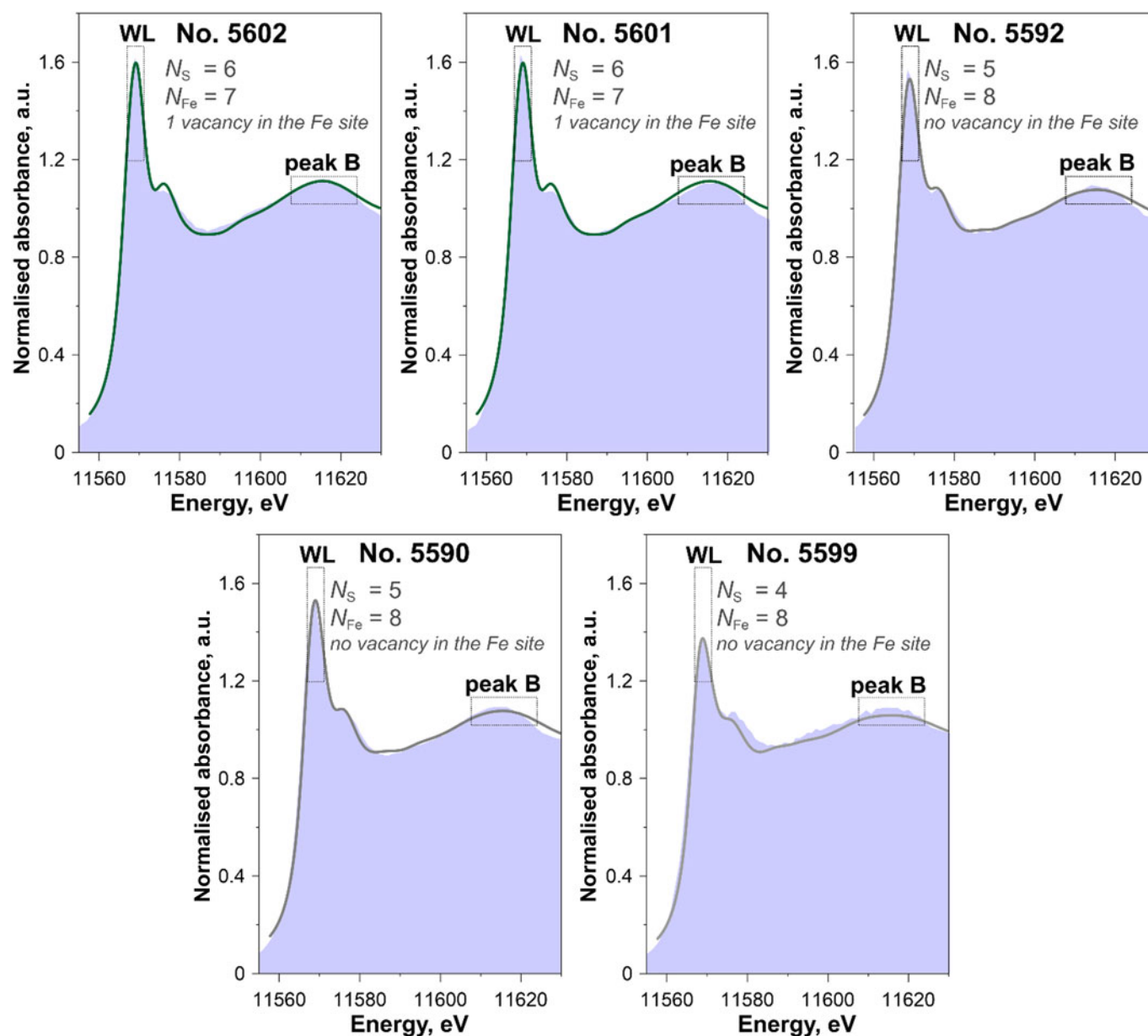


Fig. 9. Experimental Pt L_3 -edge XANES spectra of samples studied (blue fields) shown together with the spectra of the 'best' models calculated by FDMNES code (solid lines) (the 'best' models are given in Table 5, all calculations are shown in Supplementary Fig. A.3). Experimental spectra Nos. 5602 and 5601 are best described by a model with Pt surrounded by 6 S atoms in the first coordination shell and 7 Fe atoms in the second coordination shell (vacancy in the Fe site at $R_{\text{Pt-Fe}} = 3.43 \text{ \AA}$), Nos. 5590 and 5592 have 5 S atoms in the first coordination shell and 8 Fe atoms in the second coordination shell and No. 5599 has 4 S atoms in the first coordination shell and 8 Fe atoms in the second coordination shell.

Table 5. The 'best' models of Pt local atomic environment of studied pyrrhotite samples determined by means of the FDMNES simulations of Pt L_3 -edge XANES spectra.

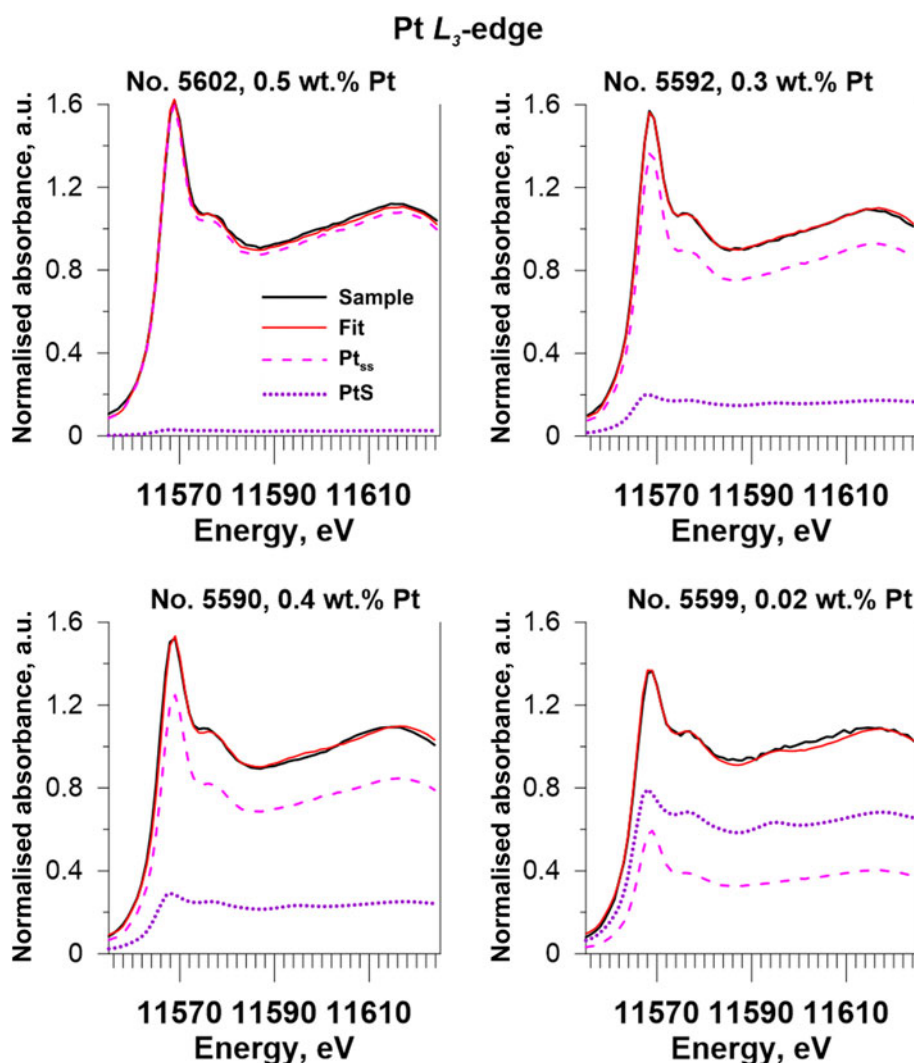
Sample ID	The 'best' models as determined by FDMNES calculations	
	First coordination sphere	Second coordination sphere
Nos. 5601 and 5602	6 S atoms	7 Fe atoms (one vacancy in the Fe site at $R_{\text{Pt-Fe}} = 3.43 \text{ \AA}$)
Nos. 5592 and 5590	5 S atoms	8 Fe atoms
No. 5599	4 S atoms	8 Fe atoms

solid solution Pt) and $\text{PtS}_{(\text{cr})}$ as the reference materials. The former was chosen because, according to the analysis of the EXAFS spectra and FDMNES simulations, this sample appeared to contain only Pt in the solid-solution state, which means that the sample was free of PtS -like clusters. The results of the analysis are presented in Table 6 and shown in Fig. 10. Sample No. 5602 contains Pt mostly in the solid-solution state ($\sim 0.5 \text{ wt.}\%$ Pt), and the contribution of PtS -like clusters is insignificant. Pyrrhotite samples No. 5590 and 5592 contain up to 0.3 wt.% Pt in the solid-solution state and up to 800 ppm Pt in the PtS -like clusters ($\sim 25\%$ of the total Pt amount). Sample No. 5599 contains $\sim 60 \text{ ppm}$ Pt in the solid-solution state and $\sim 120 \text{ ppm}$ Pt in the PtS -like clusters ($\sim 65\%$ of the total amount). In general, with increasing sulfur

Table 6. Results of Linear Combination Fit (LCF) analysis of Pt L_3 -edge XANES spectra in $\mu(E)$ space performed using the *Athena* program. Uncertainties are calculated by *Athena*.

Sample ID	Synthesis temperature (°C)	Sulfur fugacity ^a ($\log f_{S_2}$)	Average Pt content (wt.%)	Empirical formula	LCF analysis ^b		
					Pt _{PtS} (%) ^c	Pt _{ss} (%) ^c	Reduced χ^2 ; R-factor
No. 5592	650	-0.8	0.3	(Fe,Pt) _{0.89} S	2±2	98±2	<0.001; 0.001
No. 5590	650	-0.8	0.4	(Fe,Pt) _{0.89} S	16±1	84±1	<0.001; 0.001
No. 5599	650	-7.0	0.017	(Fe,Pt) _{0.975} S	23±3	77±3	<0.001; 0.001
					64±3	36±3	<0.001; 0.001

^aSulfur fugacity was determined using diagram shown in Fig. 4; ^benergy range 11,550–11,625 eV; ^cPt_{PtS} – PtS fraction, Pt_{ss} – Pt solid-solution fraction.

**Fig. 10.** Results obtained via Linear Combination Fit (LCF) modelling of Pt-bearing pyrrhotites XANES spectra. Solid black lines – experiment, solid red lines – fit results, dashed pink lines – Pt in the solid solution (Pt_{ss}, sample No. 5601), and dotted violet lines – PtS_(cr).

fugacity, the fraction of isomorphous Pt in pyrrhotite increases from ~100 ppm to 0.3 wt.% at 650°C and 0.5 wt.% at 720°C, whereas the fraction of PtS-like clusters drops significantly with the increase of temperature from 650 to 720°C.

On the basis of our previous results obtained for Pt-bearing pyrites (Filimonova *et al.*, 2019), we consider the PtS-like clusters to be a product of the solid-solution decomposition. Thus, the results of LCF analyses show that isomorphous Pt in pyrrhotite synthesised at relatively high sulfur fugacity at $T = 720^\circ\text{C}$ (sample No. 5602) withstands cooling. At the same time, the cooling of

pyrrhotite obtained at relatively low sulfur fugacity at $T = 650^\circ\text{C}$ (sample No. 5599) results in partial decomposition of isomorphous solid solution and redistribution of Pt into the PtS-like clusters.

Conclusions and implications

To determine the state of Pt in pyrrhotite in the present study, we synthesised pyrrhotite samples with Pt content from 0.004 to

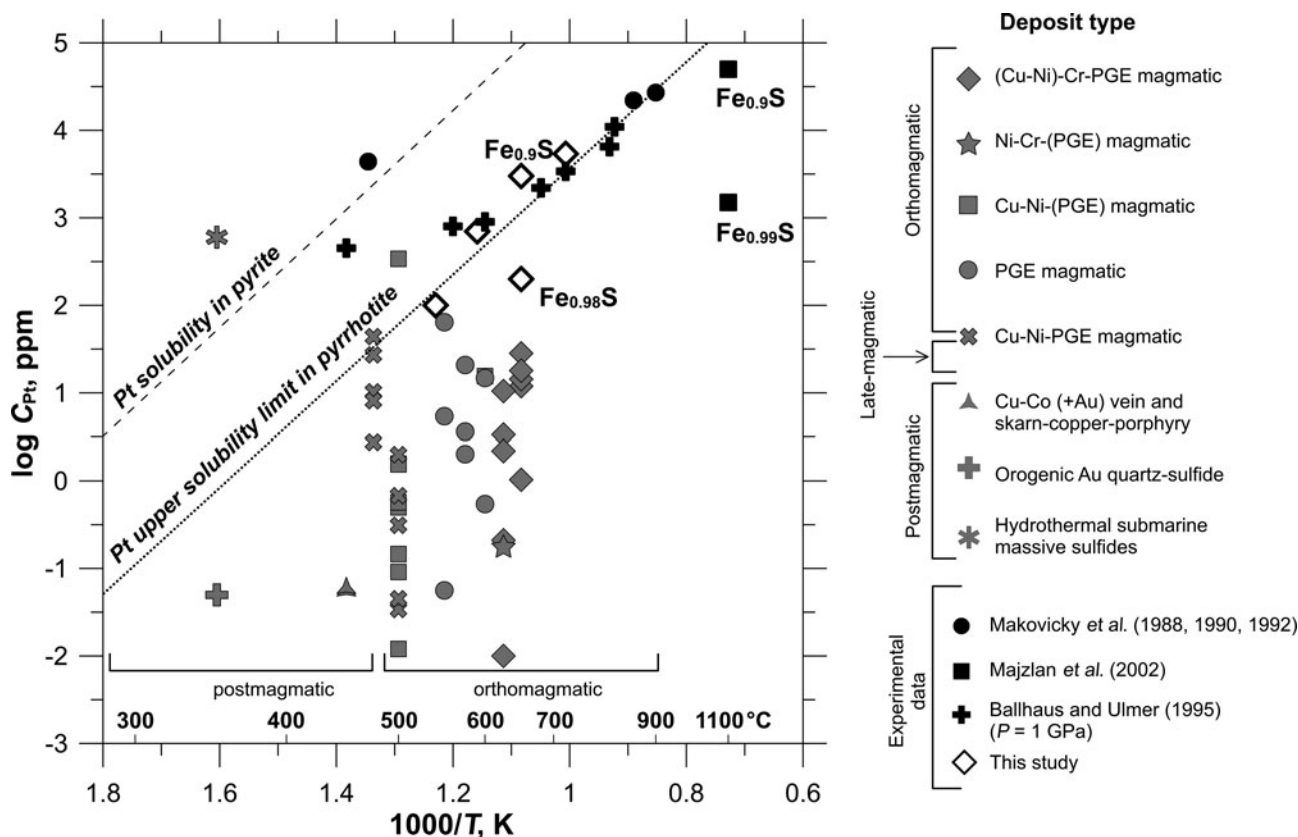


Fig. 11. The content of Pt in pyrrhotite as a function of the approximate formation temperature. Pyrrhotite sketch diagram is built using literature data from Table 1 and experimental data of this study given in Table 2 and Supplementary Table A.3. The solid line shows the inferred solubility limit of Pt in pyrrhotite. The values, which lie above the line, are presumed to be oversaturated with respect to isomorphous Pt. The solubility of Pt in pyrite adopted from Filimonova et al. (2019) is shown by the dashed line for comparison.

0.12 at.%. Analysis of Pt L_3 -edge XANES spectra revealed two groups of samples with different states of Pt. In the first group Pt exists mostly in the 4+ 'formal' oxidation state. The second group of samples contain admixture (up to ~20% of total Pt) of Pt^{2+} . Additionally, one sample contains Pt in 4+ and 2+ 'formal' oxidation states in similar concentrations. Theoretical modelling of XANES and interpretation of EXAFS spectra showed that Pt^{4+} substitutes for Fe in the crystal structure of pyrrhotite, whereas Pt^{2+} forms PtS-like clusters disseminated in the pyrrhotite matrix. It was found that an increase of f_{S_2} resulted in an increase of Pt content in pyrrhotite. At high sulfur fugacity up to 0.5 wt.% Pt substitutes for Fe in the pyrrhotite structure (temperature $\approx 700^\circ\text{C}$, the system is saturated with respect to $PtS_{(cr)}$). Additionally, when the sulfur fugacity in the experimental system was high ($-0.8 < \log f_{S_2} < -0.1$ at 700°C , determined using f_{S_2} - $1000/T$ diagram from Toulmin and Barton, 1964), the Pt-bearing isomorphous solid solution withstood subsequent cooling to ambient temperature. At relatively low sulfur fugacity, the cooling of pyrrhotite resulted in partial decomposition of the isomorphous solid solution. In our samples synthesised in the systems of low sulfur fugacity, up to 20% of Pt ($\log f_{S_2} \sim -0.8$) and 60% of Pt ($\log f_{S_2} \sim -7.0$) were redistributed into the PtS-like clusters with a decrease of temperature. Both the increase of the Pt concentration and the absence of decomposition of the Pt solid solution during cooling in the systems with high sulfur fugacity imply that the high f_{S_2} stabilises Pt in pyrrhotite in the solid-solution state.

As determined by Pt L_3 -edge EXAFS spectra fitting, an atom of isomorphous Pt in pyrrhotite is surrounded by 6 S atoms at a

distance of $\sim 2.39 \text{ \AA}$. Despite the closeness of Pt^{4+} and Fe^{2+} ionic radii (0.625 \AA of Pt vs. 0.61 \AA of Fe, Shannon, 1976), the $Me-S$ distance decreased from 2.43 to 2.39 \AA when Pt substituted for Fe in the pyrrhotite structure. The Pt-S interatomic distance obtained is close to that in PtS_2 ($N_S = 6$, $R_{Pt-S} = 2.39 \text{ \AA}$), however the absence of a notable contribution from the distant coordination shells around the absorbing Pt atom implies that this form of Pt is different from PtS_2 inclusions and can be ascribed to the isomorphous solid solution. The weak contribution of the distant coordination shell atoms to the EXAFS signal can be accounted for by the complex incommensurate crystal structure of pyrrhotite. Several samples exhibited the decrease of the Pt first sphere coordination number and interatomic distances relative to the isomorphous Pt; in one sample a substantial increase of the Debye-Waller parameter was observed. These facts can be explained by the presence of PtS-like clusters (for $PtS_{(cr)}$ $N_S = 4$ and $R_{Pt-S} = 2.3 \text{ \AA}$, Table 4).

Results of theoretical FDMNES simulations of XANES spectra are consistent with the data obtained by means of LCF XANES and EXAFS fitting. The XANES spectra of samples synthesised at high f_{S_2} , where the isomorphous solid solution predominates, are best described by a model with 6 S atoms surrounding the excited Pt atom in the first coordination sphere and 7 Fe atoms in the second sphere at 3.43 \AA (one vacancy in the Fe sublattice). Due to the presence of the PtS-like clusters in other samples, synthesised at low f_{S_2} , the average number of S atoms surrounding the excited Pt atom decreased to 5 ($\log f_{S_2} \sim -0.8$, $T = 650^\circ\text{C}$) and to 4 ($\log f_{S_2} \sim -7.0$, $T = 650^\circ\text{C}$). In samples with the PtS-like

clusters, a vacancy in the Fe sublattice was not observed. However, the effect of the vacancy on the XAS signal can be masked by the contribution from the PtS-like clusters. Therefore, only samples with negligible content of PtS-like clusters provide unambiguous information about the composition of the second coordination sphere of Pt, where one vacancy at the Fe site was detected.

In general, the results of XAS spectroscopy and *ab initio* FDMNES modelling demonstrate that sulfur fugacity and temperature control the solubility of Pt in pyrrhotite. Compilation of the present study results and literature data on the concentration of Pt in synthetic and natural pyrrhotites (Fig. 11) shows that a decrease in temperature leads to a significant drop in Pt solubility. The maximum content of the solid-solution Pt in pyrrhotite can be approximated by a straight line in the $\log C(\text{Pt})$ vs. $1/T$ plot. According to data presented in Fig. 11, the solubility limit of Pt in pyrrhotite increases from 1 ppm at 350°C to 3 wt.% at 900°C. As pyrrhotite is commonly the main base-metal sulfide, dominating among the ore minerals, the solid-solution Pt makes a noticeable contribution to the total balance of platinum, especially in high-temperature PGE and nickel/ Cu-Ni sulfide ores. It is interesting to note that the effect of temperature on the solubility of Pt in pyrite and pyrrhotite is described by parallel lines, with the solubility in pyrite being ~50 times higher than the Pt solubility limit in pyrrhotite.

Acknowledgements. The authors thank the ESRF for the beamtime allocation under proposal No. 20-01-782 (ROBL). We thank V. Abramova for the analyses of synthesised minerals using LA-ICP-MS. Chemical analyses were performed at the "IGEM-Analytica" Center for Collective Use (EPMA, SEM). We thank A. Shiryayev for inclusion of our samples in the ESRF experiment, and for the analyses of synthesised minerals using XRD in the Center of Collective Use for Physical Analytical Methods, Frumkin Institute of Physical Chemistry and Electrochemistry, RAS. The helpful comments of two anonymous reviewers are gratefully acknowledged. The study was supported by the Russian Science Foundation grant No. 20-17-00184 (XAS experiment, theoretical spectra simulations, interpretation of the experimental and theoretical data); Russian Foundation for Basic Research grant No. 20-35-70049 (synthesis experiments and chemical analyses of the synthetic crystals); Russian Foundation for Basic Research grant No. 20-05-00849 (collection and interpretation of natural ore compositions); and Russian Ministry of Science and Education grant No. 075-15-2019-1891 (XAS experimental set-up).

Supplementary material. To view supplementary material for this article, please visit <https://doi.org/10.1180/mgm.2021.76>

References

- Amaral L.F.S. (2017) *The Distribution of Platinum-Group Elements and Other Chalcophile Elements Among Sulfide Minerals from the Ovoid Ore Body of the Voisey's Bay Ni-Cu Sulfide Deposit, Canada*. MSc thesis, Université du Québec à Chicoutimi, Canada.
- Ballhaus C. and Ulmer P. (1995) Platinum-group elements in the Merensky Reef: II. Experimental solubilities of platinum and palladium in Fe_{1-x}S from 950 to 450°C under controlled $f\text{S}_2$ and $f\text{H}_2$. *Geochimica et Cosmochimica Acta*, **59**, 4881–4888.
- Barnes S.J. and Ripley E.M. (2016) Highly siderophile and strongly chalcophile elements in magmatic ore deposits. Pp. 725–774 in: *Highly Siderophile and Strongly Chalcophile Elements in High Temperature Geochemistry and Cosmochemistry* (J. Havey and J.M. Day, editors). Reviews in Mineralogy and Geochemistry, **81**. Mineralogical Society of America and the Geochemical Society, Chantilly, Virginia, USA.
- Barnes S.J., Cox R.A. and Zientek M.L. (2006) Platinum-group element, gold, silver and base metal distribution in compositionally zoned sulfide droplets from the Medvezky Creek Mine, Noril'sk, Russia. *Contributions to Mineralogy and Petrology*, **152**, 187–200.
- Barnes S.-J., Prichard H.M., Cox R.A., Fisher P.C. and Godel B. (2008) The location of the chalcophile and siderophile elements in platinum-group element ore deposits (a textural, microbeam and whole rock geochemical study): implications for the formation of the deposits. *Chemical Geology*, **248**, 295–317.
- Bogdanov Yu.A., Sagalevich A.M., Gurvich E.G., Vikent'ev I.V., Lein A.Yu., Pimenov N.V., Rudenko M.V., Peresyplkin V.I., Gordeev V.Yu. and Voitov D.V. (1999) Submarine geological studies at the Rainbow hydrothermal field, Mid-Atlantic Ridge. *Doklady Earth Sciences*, **365**, 309–314.
- Bogdanov Yu.A., Bortnikov N.S., Vikent'ev I.V., Lein A.Yu., Gurvich E.G., Sagalevich A.M. and Apollonov V.N. (2002) Mineralogical-geochemical peculiarities of hydrothermal sulfide ores and fluids in the Rainbow field associated with serpentinites, Mid-Atlantic ridge (36°14' N). *Geology of Ore Deposits*, **44**, 510–543.
- Brostigen G. and Kjekshus A. (1969) Redetermined crystal structure of FeS_2 (pyrite). *Acta Chemica Scandinavica*, **23**, 2186–2188.
- Cabri L.J. (1992) The distribution of trace precious metals in minerals and mineral products. *Mineralogical Magazine*, **56**, 289–308.
- Cabri L.J., Sylvester P.L., Tubrett M.N., Peregoedova A. and Laflamme J.H.G. (2003) Comparison of LAM-ICP-MS and micro-PIXE results for palladium and rhodium in selected samples of Noril'sk and Talnakh sulfides. *The Canadian Mineralogist*, **41**, 321–329.
- Cabri L.J., Rudashevsky N.S. and Rudashevsky V.N. (2008) Current approaches for the process mineralogy of platinum-group element ores and tailings. 9th *International Congress for Applied Mineralogy ICAM*, 9–17.
- Cabri L.J., Choi Y., Nelson M., Tubrett M. and Sylvester P.J. (2010) Advances in precious metal trace element analyses for department using LA-ICPMS. *Proceedings of the 42nd Annual Canadian Mineral Processors Conference*, 181–196.
- Chareev D.A. (2016) General principles of the synthesis of chalcogenides and pnictides in salt melts using a steady-state temperature gradient. *Crystallography Reports*, **61**, 506–511.
- Chareev D.A., Volkova O.S., Geringer N.V., Koshelev A.V., Nekrasov A.N., Osadchii V.O., Osadchii E.G. and Filimonova O.N. (2016) Synthesis of chalcogenide and pnictide crystals in salt melts using a steady-state temperature gradient. *Crystallography Reports*, **61**, 682–691.
- Chen L.-M., Song X.-Y., Danyushevsky L.V., Wang Y.-S., Tian Y.-L. and Xiao J.-F. (2015) A laser ablation ICP-MS study of platinum-group and chalcophile elements in base metal sulfide minerals of the Jinchuan Ni-Cu sulfide deposit, NW China. *Ore Geology Reviews*, **65**, 955–967.
- Dare S.A., Barnes S.J. and Prichard H.M. (2010) The distribution of platinum group elements (PGE) and other chalcophile elements among sulfides from the Creighton Ni-Cu-PGE sulfide deposit, Sudbury, Canada, and the origin of palladium in pentlandite. *Mineralium Deposita*, **45**, 765–793.
- Dare S.A., Barnes S.J., Prichard H.M. and Fisher P.C. (2011) Chalcophile and platinum-group element (PGE) concentrations in the sulfide minerals from the McCreeley East deposit, Sudbury, Canada, and the origin of PGE in pyrite. *Mineralium Deposita*, **46**, 381–407.
- Dare S.A.S., Barnes S.-J., Prichard H.M. and Fisher P.C. (2014) Mineralogy and geochemistry of Cu-rich ores from the McCreeley East Ni-Cu-PGE Deposit (Sudbury, Canada): Implications for the behavior of platinum group and chalcophile elements at the end of crystallization of a sulfide liquid. *Economic Geology*, **109**, 343–366.
- Distler V.V., Malevsky A.Y. and Laputina I.P. (1977) Distribution of platinoids between pyrrhotite and pentlandite during crystallization of the sulfide melt. *Geokhimiya*, **11**, 1646–1658 [in Russian]
- Distler V.V., Sluzhenikin S.F., Cabri L.J., Krivolutskaia N.A., Turovtsev D.M., Golovanova T.A., Mokhov A.V., Knauf V.V. and Oleshkevich O.I. (1999) Platinum ores of the Noril'sk layered intrusions: magmatic and fluid concentration of noble metals. *Geology of Ore Deposits*, **41**, 214–237.
- Djon M.L.N. and Barnes S.-J. (2012) Changes in sulfides and platinum-group minerals with the degree of alteration in the Roby, Twilight, and High Grade Zones of the Lac des Iles Complex, Ontario, Canada. *Mineralium Deposita*, **47**, 875–896.
- Duran C.J., Barnes S.-J. and Corkery J.T. (2016) Trace element distribution in primary sulfides and Fe-Ti oxides from the sulfide-rich pods of the Lac des Iles Pd deposits, Western Ontario, Canada: Constraints on processes

- controlling the composition of the ore and the use of pentlandite compositions in exploration. *Journal of Geochemical Exploration*, **166**, 45–63.
- Evstigneeva P.V., Trigub A.L., Chareev D.A., Nickolsky M.S. and Tagirov B.R. (2021) The charge state of Pt in binary compounds and synthetic minerals determined by X-ray absorption spectroscopy and quantum chemical calculations. *Minerals*, **11**, 79.
- Filimonova O.N., Nickolsky M.S., Trigub A.L., Chareev D.A., Kvashnina K.O., Kovalchuk E.V., Vikentyev I.V. and Tagirov B.R. (2019) The state of platinum in pyrite studied by X-ray absorption spectroscopy of synthetic crystals. *Economic Geology*, **114**, 1649–1663.
- Galoisy L. (2004) X-ray absorption spectroscopy in geosciences: Information from the EXAFS region. Pp. 553–587 in: *Spectroscopic Methods in Mineralogy* (Beran, A. and Libowitzky, E., editors). EMU Notes in Mineralogy, **6**.
- Godel B. and Barnes S.-J. (2008) Platinum-group elements in sulfide minerals and the whole rocks of the J-M Reef (Stillwater Complex): Implications for the formation of the reef. *Chemical Geology*, **248**, 272–294.
- Godel B., Barnes S.-J. and Maier W.D. (2007) Platinum-group elements in sulfide minerals, platinum-group minerals, and whole-rocks of the Merensky Reef (Bushveld Complex, South Africa): Implications for the formation of the reef. *Journal of Petrology*, **48**, 1569–1604.
- Guda S.A., Guda A.A., Soldatov M.A., Lomachenko K.A., Bugaev A.L., Lamberti C., Gawelda W., Bressler C., Smolentsev G., Soldatov A.V. and Joly Y. (2015) Optimized finite difference method for the full-potential XANES simulations: application to molecular adsorption geometries in MOFs and metal–ligand intersystem crossing transients. *Journal of Chemical Theory and Computation*, **11**, 4512–4521.
- Hedin L. and Lundqvist B.I. (1971) Explicit local exchange-correlation potentials. *Journal of Physics C: Solid State Physics*, **4**, 2064.
- Holwell D.A. and McDonald I. (2007) Distribution of platinum-group elements in the Platreef at Overysel, northern Bushveld Complex: a combined PGM and LA-ICP-MS study. *Contributions to Mineralogy and Petrology*, **154**, 171–190.
- Holwell D.A., Adeyemi Z., Ward L.A., Smith D.J., Graham S.D., McDonald I. and Smith J.W. (2017) Low temperature alteration of magmatic Ni–Cu–PGE sulfides as a source for hydrothermal Ni and PGE ores: A quantitative approach using automated mineralogy. *Ore Geology Reviews*, **91**, 718–740.
- Hutchinson D. and McDonald I. (2008) Laser ablation ICP-MS study of platinum-group elements in sulfides from the Platreef at Turfspruit, northern limb of the Bushveld Complex, South Africa. *Mineralium Deposita*, **43**, 695–711.
- Joly Y. (2001) X-ray absorption near-edge structure calculations beyond the muffin-tin approximation. *Physical Review*, **B63**, 125120.
- Knight R.D., Prichard H.M. and Ferreira Filho C.F. (2017) Evidence for As contamination and the partitioning of Pd into pentlandite and Co + platinum group elements into pyrite in the Fazenda Mirabela Intrusion, Brazil. *Economic Geology*, **112**, 1889–1912.
- Large R.R., Maslennikov V.V., Robert F., Danyushevsky L.V. and Chang Z. (2007) Multistage sedimentary and metamorphic origin of pyrite and gold in the giant Sukhoi Log deposit, Lena gold province, Russia. *Economic Geology*, **102**, 1233–1267.
- Majzlan J., Makovicky M., Makovicky E. and Rose-Hansen J. (2002) The system Fe–Pt–S at 1100°C. *The Canadian Mineralogist*, **40**, 509–517.
- Makovicky M., Makovicky E. and Rose-Hansen J. (1988) Experimental evidence on the formation and mineralogy of platinum and palladium ore deposits. Pp. 303–317 in: *Mineral Deposits within the European Community*. Springer, Berlin–Heidelberg.
- Makovicky E., Karup-Møller S., Makovicky M. and Rose-Hansen J. (1990) Experimental studies on the phase systems Fe–Ni–Pd–S and Fe–Pt–Pd–As–S applied to PGE deposits. *Mineralogy and Petrology*, **42**, 307–319.
- Makovicky M., Makovicky E. and Rose-Hansen J. (1992) The phase system Pt–Fe–As–S at 850°C and 470°C. *Neues Jahrbuch für Mineralogie Monatshefte*, **10**, 441–453.
- Malevsky A.Y., Laputina I.P. and Distler V.V. (1977) Behaviour of platinum metals at pyrrhotite crystallization from sulfide melt. *Geochemistry*, **10**, 1534–1542.
- Mansur E.T. and Barnes S.-J. (2020) The role of Te, As, Bi, Sn and Sb during the formation of PGE deposits: examples from the Bushveld and Stillwater Complexes. *Geochim Cosmochim Acta*, **272**, 235–258.
- Mansur E.T., Barnes S.-J., Duran C.J. and Sluzhenikin S.F. (2020) Distribution of chalcophile and platinum-group elements among pyrrhotite, pentlandite, chalcopyrite and cubanite from the Noril'sk-Talnakh ores: implications for the formation of platinum-group minerals. *Mineralium Deposita*, **55**, 1215–1232.
- Mansur E.T., Barnes S.-J. and Duran C.J. (2021) An overview of chalcophile element contents of pyrrhotite, pentlandite, chalcopyrite and pyrite from magmatic Ni–Cu–PGE sulfide deposits. *Mineralium Deposita*, **56**, 179–204.
- Mills K.C. (1974) *Thermodynamic Data for Inorganic Sulfides, Selenides and Tellurides*. John Wiley and Sons, Incorporated.
- Mottana A. (2004) X-ray absorption spectroscopy in mineralogy: Theory and experiment in the XANES region. Pp. 465–522 in: *Spectroscopic Methods in Mineralogy* (Beran, A. and Libowitzky, E., editors). EMU Notes in Mineralogy, **6**.
- Murzina V.V., Varlamov D.A. and Vikentyev I.V. (2011) Copper-cobalt mineralization of the Pyshminsk-Klyuchevsk deposit in the Middle Urals: Mineral composition of ore and metasomatites, stages, P–T conditions of mineral formation. *Lithosphere*, **6**, 103–122 [in Russian].
- Naumov G.B., Ryzhenko B.N. and Khodakovskiy I.L. (1974) *Handbook of Thermodynamic Data*. Springfield, Virginia, USA.
- Oberthür T., Cabri L.J., Weiser T.J., McMahon G. and Mueller P. (1997) Pt, Pd and other trace elements in sulfides of the Main Sulfide Zone, Great Dyke, Zimbabwe; a reconnaissance study. *The Canadian Mineralogist*, **35**, 597–609.
- Osbahr I., Klemd R., Oberthür T., Brätz H. and Schouwstra R. (2013) Platinum-group element distribution in base-metal sulfides of the Merensky Reef from the eastern and western Bushveld Complex, South Africa. *Mineralium Deposita*, **48**, 211–232.
- Osbahr I., Oberthür T., Klemd R. and Josties A. (2014) Platinum-group element distribution in base-metal sulfides of the UG2 chromitite, Bushveld Complex, South Africa – a reconnaissance study. *Mineralium Deposita*, **49**, 655–665.
- Paton C., Hellstrom J., Paul B., Woodhead J. and Hergt J. (2011) Iolite: Firmware for the visualisation and processing of mass spectrometric data. *Journal of Analytical Atomic Spectrometry*, **26**, 2508–2518.
- Piña R., Gervilla F., Barnes S.J., Ortega L. and Lunar R. (2012) Distribution of platinum-group and chalcophile elements in the Aguablanca Ni–Cu sulfide deposit (SW Spain): evidence from a LA-ICP-MS study. *Chemical Geology*, **302**, 61–75.
- Piña R., Gervilla F., Barnes S.J., Ortega L. and Lunar R. (2013) Partition coefficients of platinum group and chalcophile elements between arsenide and sulfide phases as determined in the Beni Bousera Cr–Ni mineralization (North Morocco). *Economic Geology*, **108**, 935–951.
- Piña R., Gervilla F., Barnes S.J., Oberthür T. and Lunar R. (2016) Platinum-group element concentrations in pyrite from the Main Sulfide Zone of the Great Dyke of Zimbabwe. *Mineralium Deposita*, **51**, 853–872.
- Putz H. and Brandenburg K. (2012) *Diamond V. 3.2*. Crystal Impact, Kreuzherrenstr, Bonn, Germany.
- Ravel B. and Newville M. (2005) Athena, Artemis, Hephaestus: data analysis for X-ray absorption spectroscopy using IFEFFIT. *Journal of Synchrotron Radiation*, **12**, 537–541.
- Rozhdestvina V.I., Ivanov A.V., Zarembo M.A., Antsutkin O.N. and Forsling W. (2008) Single-crystalline cooperite (PtS): Crystal-chemical characterization, ESR spectroscopy, and 195Pt NMR spectroscopy. *Crystallography Reports*, **53**, 391–397.
- Samalens N., Barnes S.-J. and Sawyer E.W. (2017) A laser ablation inductively coupled plasma mass spectrometry study of the distribution of chalcophile elements among sulfide phases in sedimentary and magmatic rocks of the Duluth Complex, Minnesota, USA. *Ore Geology Reviews*, **90**, 352–370.
- Shannon R.D. (1976) Revised effective ionic radii and systematic studies of interatomic distances in halides and chalcogenides. *Acta Crystallographica*, **A32**, 751–767.
- Sluzhenikin S.F., Distler V.V., Dyuzhikov O.A., Kravtsov V.F., Kunilov V.E., Laputina I.P. and Turovtsev D.M. (1994) Low-sulfide platinum mineralization of the Norilsk layered intrusions. *Geology of Ore Deposits*, **36**, 195–217 [in Russian].

- Sluzhenikin S.F., Distler V.V. and Grigor'eva A.B. (2015) Breccia ores of Oktyabrsk deposit as a perspective source of platinum metals (Norilsk district). *Proceedings of the Conference on Deposits of Strategic Metals: Regularities of Location, Sources of Substance, Conditions and Mechanisms of Formation*, 239–240 [in Russian].
- Sluzhenikin S.F., Yudovskaya M.A., Barnes S.J., Abramova V.D., Le Vaillant M., Petrenko D.B., Grigor'eva A.V. and Brovchenko V.D. (2020) Low-sulfide platinum group element ores of the Norilsk-Talnakh Camp. *Economic Geology*, **115**, 1267–1303.
- Smith J.W., Holwell D.A. and McDonald I. (2014) Precious and base metal geochemistry and mineralogy of the Grasvalley Norite-Pyroxenite-Anorthosite (GNPA) member, northern Bushveld Complex, South Africa: implications for a multistage emplacement. *Mineralium Deposita*, **49**, 667–692.
- Toulmin P. and Barton P. (1964) A thermodynamic study of pyrite and pyrrhotite. *Geochimica et Cosmochimica Acta*, **28**, 641–671.
- Trubač J., Ackerman L., Gauert C., Đurišová J. and Hrstka T. (2018) Platinum-group elements and gold in base metal sulfides, platinum-group minerals, and Re-Os isotope compositions of the Uitkomst Complex, South Africa. *Economic Geology*, **113**, 439–461.
- Vikent'ev I.V., Murzin V.V., Prokofev V.Yu., Dubinina E.O. and Eremin N.I. (2010) PT conditions of mineral formation and characteristics of fluid of the Pyshminsk-Klyuchevsk copper-cobalt deposit, Middle Urals. *Doklady Earth Sciences*, **430**, 214–217.
- Vikentyev I.V., Grabezhev A.I., Moloshag V.P., Novokreschenov S.M. and Neustroeva I.I. (2005) PGE in the ores of magnetite-copper-skarn deposits of the Urals. *Zavaritsky Institute of Geology and Geochemistry, Yekaterinburg, Russia*, **2004**, 328–331 [in Russian].
- Wilson S.A., Ridley W.I. and Koenig A.E. (2002) Development of sulfide calibration standards for the laser ablation inductively-coupled plasma mass spectrometry technique. *Journal of Analytical Atomic Spectrometry*, **17**, 406–409.
- Wohlgemuth-Ueberwasser C.C., Ballhaus C., Berndt J., Stotter née Paliulionyte V. and Meisel T. (2007) Synthesis of PGE sulfide standards for laser ablation inductively coupled plasma mass spectrometry (LA-ICP-MS). *Contributions to Mineralogy and Petrology*, **154**, 607–617.
- Wyckoff R.W.G. (1963) *Crystal Structures*. Vol. 1. Interscience Publishers, New York [pp. 85–237].
- Yudovskaya M.A., Kinnaird J.A., Grobler D.F., Costin G., Abramova V.D., Dunnett T., Barnes S.-J. (2017) Zonation of Merensky-style platinum-group element mineralization in Turfspruit Thick Reef Facies (Northern Limb of the Bushveld Complex). *Economic Geology*, **112**, 1333–1365.
- Zabinsky S.I., Rehr J.J., Ankudinov A., Albers R.C. and Eller M.J. (1995) Multiple-scattering calculations of X-ray-absorption spectra. *Physical Review*, **B52**, 2995.
- Zaccarini F., Garuti G., Fiorentini M.L., Locmelis M., Kollegger P. and Thalhammer O.A. (2014) Mineralogical hosts of platinum group elements (PGE) and rhenium in the magmatic Ni-Fe-Cu sulfide deposits of the Ivrea Verbano Zone (Italy): an electron microprobe study. *Neues Jahrbuch für Mineralogie-Abhandlungen. Journal of Mineralogy and Geochemistry*, **191**, 169–187.
- Zelenski M., Kamenetsky V.S., Mavrogenes J.A., Danyushevsky L.V., Matveev D. and Gurenko A.A. (2017) Platinum-group elements and gold in sulfide melts from modern arc basalt (Tolbachik volcano, Kamchatka). *Lithos*, **290–291**, 172–188.